Remote Sensing of Environment 283 (2022) 113325

Contents lists available at ScienceDirect

Remote Sensing of Environment

journal homepage: www.elsevier.com/locate/rse

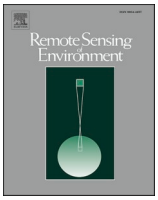

A comprehensive multiparametric and multilayer approach to study the preparation phase of large earthquakes from ground to space: The case study of the June 15 2019, M7.2 Kermadec Islands (New Zealand) earthquake

A. De Santis [a,*], L. Perrone [a], M. Calcara [a], S.A. Campuzano [b], G. Cianchini [a], S. D'Arcangelo [a,c], D. Di Mauro [a], D. Marchetti [d], A. Nardi [a], M. Orlando [a], A. Piscini [a], D. Sabbagh [a], M. Soldani [a]

[a] Istituto Nazionale di Geofisica e Vulcanologia, 00143 Rome, Italy
[b] Instituto de Geociencias IGEO (CSIC-UCM), 28040 Madrid, Spain
[c] Universidad Complutense de Madrid - UCM, 28040 Madrid, Spain
[d] College of Instrumentation and Electrical Engineering, Jilin University, 130061 Changchun, China

ARTICLE INFO

Edited by Jing M. Chen

Keywords:
Pre-earthquake anomalies
LAIC
Earthquake
Swarm satellites
CSES

ABSTRACT

This work deals with a comprehensive multiparametric and multilayer approach to study earthquake-related processes that occur during the preparation phase of a large earthquake. As a case study, the paper investigates the M7.2 Kermadec Islands (New Zealand) large earthquake that occurred on June 15, 2019 as the result of shallow reverse faulting within the Tonga-Kermadec subduction zone. The analyses focused on seismic (earthquake catalogs), atmospheric (climatological archives) and ionospheric data from ground to space (mainly satellite) in order to disclose the possible Lithosphere-Atmosphere-Ionosphere Coupling (LAIC). The ionospheric investigations analysed and compared the Global Navigation Satellite System (GNSS) receiver network with in-situ observations from space thanks to both the European Space Agency (ESA) Swarm constellation and the China National Space Administration (CNSA in partnership with Italian Space Agency, ASI) satellite dedicated to search for possible ionospheric disturbances before medium-large earthquakes, i.e. the China Seismo-Electromagnetic Satellite (CSES-01). An interesting comparison is made with another subsequent earthquake with comparable magnitude (M7.1) that occurred in Ridgecrest, California (USA) on 6 July of the same year but in a different tectonic context. Both earthquakes showed anomalies in several parameters (e.g. aerosol, skin temperature and some ionospheric quantities) that appeared at almost the same times before each earthquake occurrence, evidencing a chain of processes that collectively point to the moment of the corresponding mainshock. In both cases, it is demonstrated that a comprehensive multiparametric and multilayer analysis is fundamental to better understand the LAIC in the occasion of complex phenomena such as earthquakes.

1. Introduction

Earthquakes (EQs) release energies roughly proportional to 10^M, where M is their magnitude (e.g. Okal, 2019). The knowledge of the earthquake preparation process is a challenging task in the definition of the chain of events leading to the rupture. In case of large events, they are often made up of a sequence composed of foreshocks, mainshock and aftershocks (e.g. Mogi, 1963; Felzer et al., 2004). The recognition of all signals in the pre-seismic phase, with or without foreshocks, is the main task in earthquake prediction studies. Efforts have been made in real time foreshock phase recognition and, although some significant progress has been found in this field (e.g. McGuire et al., 2005; Gulia and Wiemer, 2019), some difficulties still remain (e.g. Dascher-Cousineau et al., 2020).

Even if one may usually consider a strategy based on seismic data analysis (e.g. De Santis et al., 2015; Cianchini et al., 2020), a non-seismic approach exists, based, for example, on the observation and detection of some anomalous behaviour of the above geolayers, i.e. atmosphere and ionosphere. This is simply justified by the fact that the lithospheric system under tectonic stress, including the earthquake preparation

* Corresponding author.
E-mail address: angelo.desantis@ingv.it (A. De Santis).

https://doi.org/10.1016/j.rse.2022.113325
Received 7 June 2022; Received in revised form 26 September 2022; Accepted 15 October 2022
Available online 28 October 2022

volume, is an open system, with, therefore, mass and energy exchange with neighbour environment, flowing, as an example, into the above atmosphere and, in turn, into the ionosphere, just during the preparation phase of the earthquake. This kind of interaction is also called Lithosphere-Atmosphere-Ionosphere Coupling (LAIC) (Hayakawa and Molchanov, 2002; Freund, 2011; Pulinets and Ouzounov, 2011). Usually, this approach takes advantage of the existence of dense ground observational networks and of currently orbiting satellites. These latter have the potential to have greater probability to be flying periodically over the seismic regions and detect any possible continuous or occasional precursors (e.g. Picozza et al., 2021).

Only recently, space missions were conducted and performed for the investigation of the circumterrestrial environment, with particular attention in observing and studying the possible coupling among solid earth, atmosphere, ionosphere and magnetosphere before strong earthquakes. The French DEMETER satellite (Parrot, 2002; Cussac et al., 2006) represented the very first attempt to put in low-Earth orbit a dedicated satellite for potential detection of ionospheric signals preceding strong earthquakes (e.g. Parrot, 2012). This satellite was flying from 2004 to 2010 and demonstrated to be able to monitor and detect ionospheric effects prior to large earthquakes (e.g. Zhima et al., 2020). Since 2013, the Swarm three-satellite mission by ESA is in progress to monitor the geomagnetic field at the best, taking advantage of the peculiar satellite orbital configuration: two satellites, Alpha and Charlie, fly at around 460 km of altitude while the third satellite, Bravo, flies at about 510 km. Its effectiveness to detect peculiar pre-earthquake anomalies of the magnetic field and electron density in the ionosphere has been lately studied and shown (De Santis et al., 2017, 2019b). The most recent space enterprise with the same objective has been the CSES-01 that was launched on 2 February 2018 and is still orbiting at about 500 km of altitude. Its on-board instruments represent the best nowadays to verify the possibility to observe anomalous behaviour of the ionosphere, possibly due to impending large earthquakes (Shen et al., 2018).

This study analyses multiparametric (seismic, atmospheric, Global Navigation Satellite System -GNSS and satellite) data trying to detect possible anomalies related to the M7.2 (as provided by GeoNet EQ catalogue, or M7.3 from USGS catalogue) Kermadec Islands (New Zealand) EQ, occurred on June 15, 2019 at 22:55:04 UTC, located at 30.644°S, 178.100°W and 46.0 km depth (USGS source: https://earthquake.usgs.gov/earthquakes/eventpage/us6000417i/executive). We also compare the results with the analogous findings of another recent seismic event, i.e. the M7.1 Ridgecrest EQ. (6 July 2019, California, USA; e.g. De Santis et al., 2020), whose open system character has been demonstrated in Pulinets et al. (2021) with the detection of an anomalous flux of radon, just days before the mainshock.

This paper is organized as follows. First, the used data are introduced, then the applied methods together with their main results are presented. Since this work is a comprehensive investigation of the EQ under study, the data analyses are made in the different geolayers from bottom to above, i.e. from lithosphere, atmosphere to ionosphere. All results are then combined and compared with those of the Ridgecrest EQ. We finally conclude with some discussion and conclusions. Although data and methods are different and heterogeneous, we attempt to provide a comprehensive and all-inclusive view of the found results, in the framework of the LAIC model. In addition, some Supplementary Material completes the work with further data analyses and results, complementary to those provided in the main text.

2. Data

In order to study the LAIC effects, several datasets are necessary. In fact, each geolayer that is investigated requires specific data from several sources. As the analysis is conducted separately in each layer, we cope with time/space different resolutions. However, the integration of the different results attempts to take into account these differences. Although some difficulties could be present to investigate the physics of the mechanism of coupling when the time or space resolution is limited, nevertheless the comparison with the results from several layers is still possible.

2.1. Lithospheric data

The seismic event under investigation was located in a very active region where one of the fastest plates (Pacific Plate) subducts beneath the Kermadec-Tonga subduction zone (Fig. 1a); here large earthquakes and volcanic eruptions are taking place (e.g. Smith and Price, 2006; D'Arcangelo et al., 2022).

The USGS catalogue (https://earthquake.usgs.gov/earthquakes/search/) and the national New Zealand catalogue, i.e. the GeoNet Earthquake Catalogue (https://www.geonet.org.nz/), were used in this study. The former catalogue has the advantage of having a global coverage due to a worldwide network of seismic stations and it has a magnitude of completeness (Mc) of about 4.5 worldwide (or even better in last years and for regions - e.g. in USA; Mueller, 2019). *Mc* is an important parameter when estimating *b*-values (Wiemer, 2000): *Mc* is the minimum magnitude for which, in a given region and temporal interval, all earthquakes with magnitude $M \geq Mc$ are recorded by the seismic network.

Since we are interested in a deeper understanding and characterisation of the specific region of New Zealand, for more detailed analyses and to achieve a lower magnitude of completeness, we retrieved the seismic data from the GeoNet site too, in the period between January 01, 2018 and June 14, 2019. The area is delimited by the Dobrovolsky strain radius (Dobrovolsky et al., 1979), that scales with magnitude M as $10^{0.43M}$ km, collecting around 18 thousand events. Although the seismic network is decentralised with respect to the epicentre (Fig. 1b), nonetheless the proximity of the northernmost station (GLKZ) assures a good detection capability in the area. The GeoNet earthquake catalogue permits to study more in detail the seismicity because the magnitude of completeness can reach 2.0, or even lower values: in particular it allows to search for some seismic "precursors" such as the variation of *b-value* (e.g. Herrmann et al., 2022) or some recognisable patterns, such as the seismic quiescence or its almost opposite, i.e. the *Accelerated Moment Release (*AMR), and its revised version, hence called R-AMR (*Revised Accelerated Moment Release;* De Santis et al., 2015). To this purpose, we downloaded the New Zealand seismic data from 2018 to the mainshock origin time in a broad region around the epicentre.

2.2. Atmospheric data

As the method of analysis is based on the comparison of the phenomenon's behaviour in the present time with that in the historical background, the downloaded data were analysed from the beginning of their availability until present, and every while we updated our archive with the most recent data. In particular, to investigate the atmosphere we retrieved several parameters, such as SKin Temperature (SKT), Total Column Water Vapour (TCWV), Outgoing Longwave Radiation (OLR), Aerosol Optical Depth (AOD), Carbon Monoxide (CO), Sulphur Dioxide (SO_2) and Methane (CH_4) from ECMWF (European Centre for Medium-range Weather Forecasts) and NASA-NOAA. Most of the data have been selected from climatological re-analysis datasets. These ones have the advantage of having a homogeneous coverage in space and time and to be only slightly altered by observation conditions, like cloud cover for satellite observations. ECMWF elaborated ERA-Interim from 1979 to 2019 and the new version ERA-5 with improvements such as temporal resolution of one hour (instead of 6 h of ERA-Interim) and more parameters and higher space resolution, updated to present in quasi-real time. NASA-NOAA elaborated the climatological model MERRA-2 (Gelaro et al., 2017). This model provides physical and chemical estimations of atmospheric conditions from 1980 to present (updated once per month). Temporal resolution is one hour and spatial resolution is

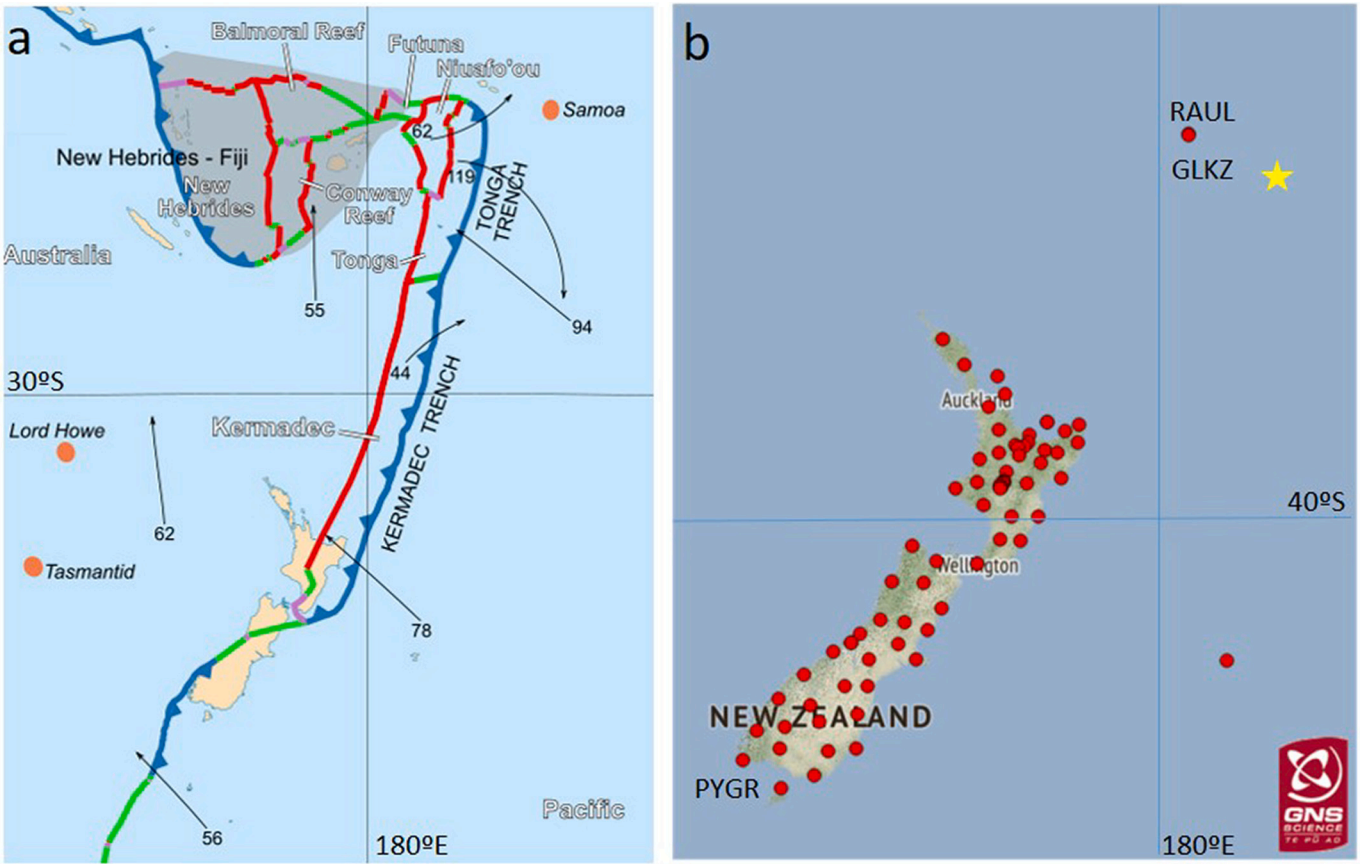

Fig. 1. (a) The Kermadec-Tonga subduction area, where the subduction direction and large velocities (the arrows and the associated velocities w.r.t. Africa in mm/yr) are evidenced. Tectonic margins are shown in red (diverging), green (transform), grey (orogens) and blue (subduction zones); red circles are seismographic stations on Islands (Image source: Wikipedia, under CC BY-SA 3.0); (b) Distribution of the seismographic stations in New Zealand: the northernmost station (GLKZ) is the closest one to the studied epicentre (Image source: GeoNet). Also two GNSS stations (RAUL, very close to the seismic station GLKZ, and PYGR) are shown: their TEC data have been used in our analysis. The yellow star shows the epicentre of the event. (For interpretation of the references to colour in this figure legend, the reader is referred to the web version of this article.)

0.625° longitude, 0.5° latitude. Both ERA-5 and MERRA-2 models were used to obtain the atmospheric parameters. We considered nighttime values because are typically less affected by local meteorological changes. The use of 40 years of data allows us to better evaluate the best background from which estimate the anomalies. The size of the geographical area investigated in the New Zealand region was determined by considering the circular earthquake preparation region (or Dobrovolsky area) centred in the earthquake epicentre (Dobrovolsky et al., 1979).

2.3. Ionospheric data

The ionospheric layer can be investigated in two ways: from in-situ observations by satellites (i.e. from satellites flying across ionosphere) and from ground observations by ionosondes and GNSS receivers. Our study addresses both approaches, mostly concentrating on CSES-01 satellite and integrating with ESA constellation Swarm three-satellites. The CSES-01 satellite is a multiplatform satellite whose main purpose is to search for ionospheric precursors of earthquakes, and for such reason it operates in "burst" mode over seismic active regions, i.e. seismic belts and China (Shen et al., 2018). We deeply investigated the plasma measurements (electron density, Ne and electron temperature, Te) from Langmuir Probes (LAP) and magnetic field measurements from High Precision Magnetometer (HPM) composed by two fluxgates and a Coupled Dark State scalar Magnetometer (CDSM) placed on one of the booms of the satellite. We also investigated the Search Coil Magnetometer (SCM) and Electric Field Detector (EFD) data from CSES-01. This satellite gives the possibility to have a good estimation of the background at two specific a.m. and p.m. local times due to its sun-synchronous orbit. For having a larger picture of the ionosphere at several local times, we integrated the magnetic field and plasma measurements from the Swarm constellation that is equipped with similar payloads with respect to CSES-01 satellite.

The CSES-01 HPM, LAP, SCM and EFD data were available at the CSES satellite web portal (www.leos.ac.cn). Regarding Swarm magnetic field data, they were downloaded as Level 1b low rate (1 Hz) data from all three satellites (up to baseline 0507) until 8 March 2020. For Swarm electron density data, we considered EFI LP (2 Hz), baseline 0501. Both datasets are provided in Common Data Format (CDF) and freely available in the ESA Swarm FTP and HTTP Server swarm-diss.eo.esa.int.

For the ground observations, we used GNSS data from the receivers of the GeoNet GNSS/GPS network (https://www.geonet.org.nz/), located within the earthquake preparation region, together with receivers outside the area of interest included for comparative analysis. The Total Electron Content (TEC), estimated from the time delay between two GPS (Global Positioning System) transmitting frequencies, can also be used to study the eventual effects in the ionosphere due to the preparation phase of strong earthquakes (e.g. Zhu and Jiang, 2020). By the other hand, a ionosonde has the advantage to determine important ionospheric parameters with the best precision, for example the altitude of the F2 layer, its limit-transmitting frequency, the eventual presence of the sporadic layer E, etcetera. Unfortunately, no ionosonde data are available from that area.

3. Data analyses and results

3.1. Seismological data analysis

The seismic data were retrieved from GeoNet Geological Information for New Zealand, in the period between 1 January 2018 and 14 June 2019 over a circular area contained by the Dobrovolsky strain radius, comprising 18,291 events. To characterise the seismicity trend, the first step was to calculate the magnitude of completeness (*Mc*). We computed *Mc* as a function of time by sliding the time window containing 150 earthquakes by steps of 5 events (Fig. 2a) and its variation in time in bold (grey lines are the upper and lower bands of confidence). Limits of the graph are set between 1 and 3, because it is the typical range of the *Mc* values from a dense seismic network.

Mc values of GeoNet network are quite stable and ranging between 1.8 and 2.2, for the time period considered. So, considering the largest value of the range, the catalogue was filtered in order to exclude all earthquakes with magnitudes lower than $Mc = 2.2$ and to obtain the *b-value* behaviour in time (Fig. 2b). The latter parameter depends on different physical and tectonic setting conditions: stress regime, heterogeneities of materials and temperature (Scholz, 2015). Low *b-values* have been correlated to asperity areas, possible origin of future earthquakes (e.g. Nanjo and Yoshida, 2021). From Fig. 2b it is worth noting a general tendence of decrease, with larger decrease at the end of 2018.

Accelerating seismicity is quite common during the preparation process of EQs. It can be detected by the Accelerated Moment Release (AMR) method, and its recent revised version (R-AMR; De Santis et al., 2015), applied to the EQ catalogue. The AMR method (e.g. Bowman et al., 1998; Bufe and Varnes, 1993) proposes that the cumulative value of the Benioff strain $s(t)$ (Benioff, 1949), which is proportional to the square root of the EQ energy, may progress following a power-law diverging function with time:

$$s(t) = \sum_{i=1}^{n(t)} \sqrt{E(t_i)} = A + B(t_f - t)^m \quad (1)$$

where $E(t_i)$ is the energy of the i-th event; $n(t)$ is the number of earthquakes at time t; $A \equiv s(t)_{|t=t_f} > 0$ at the time of failure t_f (i.e. the mainshock); $B < 0$ and $0 < m < 1$ are constant parameters, usually estimated by a non-linear least squares regression of data; m is an exponent representing the degree of accelerating energy release (De Santis et al., 2010), whose values usually are in the interval $[0.2, 0.6]$ (Mignan, 2011). The estimation of the acceleration is given by the so-called *C*-factor (Bowman et al., 1998), defined as the ratio between the root mean square (rms) of the residuals of the non-linear (power-law) fit and the root mean square of the linear fit:

$$C = \frac{rms_{nlin}}{rms_{lin}} \quad (2)$$

If C is <1, then acceleration is present, and the lower C, the more the acceleration occurs in the seismic data.

When focusing on the state of a specific fault, also the distance R_i of the i-th foreshock of the sequence from the mainshock plays an important role. De Santis et al. (2015) introduced a *revised* version of AMR (called R-AMR) to take into account the maximum distance R, supposing that the effects of preceding EQs are still perceived at the fault level, the so-called *minimum strain radius* (Dobrovolsky et al., 1979). The expression for the cumulative reduced strain becomes:

$$\underline{s}(t) = \sum_{i=1}^{n(t)} \sqrt{E(t_i)} \cdot G(R_i) \quad (3)$$

where $G(R_i)$ is an attenuation function depending on the distance R_i of the i-th EQ from the epicentre, modelled by De Santis et al. (2015) as

$$G(r) = \begin{cases} r^{-\gamma_0} & r \le R_0 \\ r^{-\gamma_1} & r > R_0 \end{cases} \quad (4)$$

where R_0 denotes the limit between two regions around the seismogenic fault, each with its own weighting exponent γ. By analysing 14 case studies worldwide, Cianchini et al. (2020) evidenced that γ_1 is generally equal to 0.5, while reasonably we set $\gamma_0 = 0$ (De Santis et al., 2015; Cianchini et al., 2020), because there is a small area around the epicentre with negligible attenuation.

The R-AMR estimates, in a sufficiently large area, the collective but surely different effect of each i-th EQ on the fault under study, according to its magnitude M_i and distance R_i from the fault. When we applied the R-AMR method (De Santis et al., 2015) to the downloaded catalogue, we observed that the seismicity accelerated during the preparation phase of the earthquake (Fig. 3). An automatic search for a significant acceleration was applied to seismic time series from the date before the EQ back to past values till C was <0.6. It is interesting to notice that the R-AMR detects a clear seismic acceleration ($C = 0.56$) when starting from middle June 2018 and predicts a magnitude similar to the real one (M(A) = 7.1 and M(B) = 7.4; see De Santis et al., 2015 or Cianchini et al., 2020 for their definitions) and a time of failure which is only around 20 days after the mainshock.

3.2. Atmospheric data analysis

In the LAIC approach, some atmospheric quantities and contents of gases have been simultaneously processed in order to identify possible persistent anomalies some days or months before the impending earthquake (Pulinets and Ouzounov, 2011). In particular, a Climatological Analysis for Seismic PRecursor Identification (CAPRI) algorithm (Piscini et al., 2017, 2019) has been applied to the ECMWF Reanalysis v5 (ERA5) and ECMWF Copernicus Atmosphere Monitoring Service (CAMS) climatological dataset with a spatial grid of 0.25° x 0.25°.

The time series of each atmospheric quantity has been collected and preprocessed in order to apply CAPRI algorithm which compares daily time series of the investigated year with the forty-year (1979–2018) historical time series in a temporal window of some months preceding

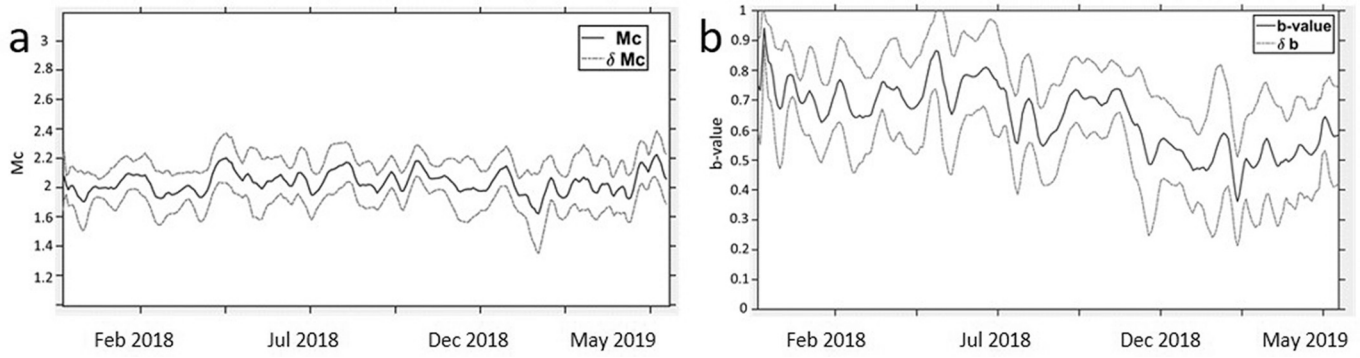

Fig. 2. Estimation of (a) Mc and (b) b-value in function of time with their bands of confidence for the earthquake of interest.

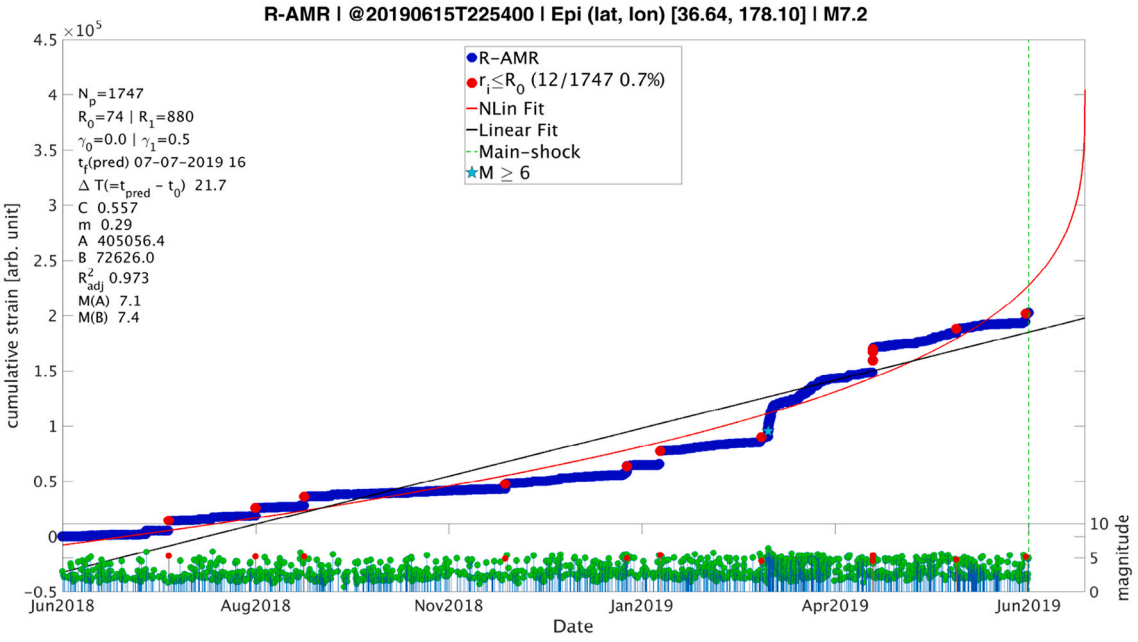

Fig. 3. The R-AMR analysis of the New Zealand catalogue around the 2019 M7.2 Kermadec Islands EQ. The algorithm evidenced an increased seismicity following a rather large foreshock (M > 6; shown as a cyan star) in March 2019, a few months before the mainshock. The figure shows also some parameters involved in the R-AMR analysis (see text for more details). (For interpretation of the references to colour in this figure legend, the reader is referred to the web version of this article.)

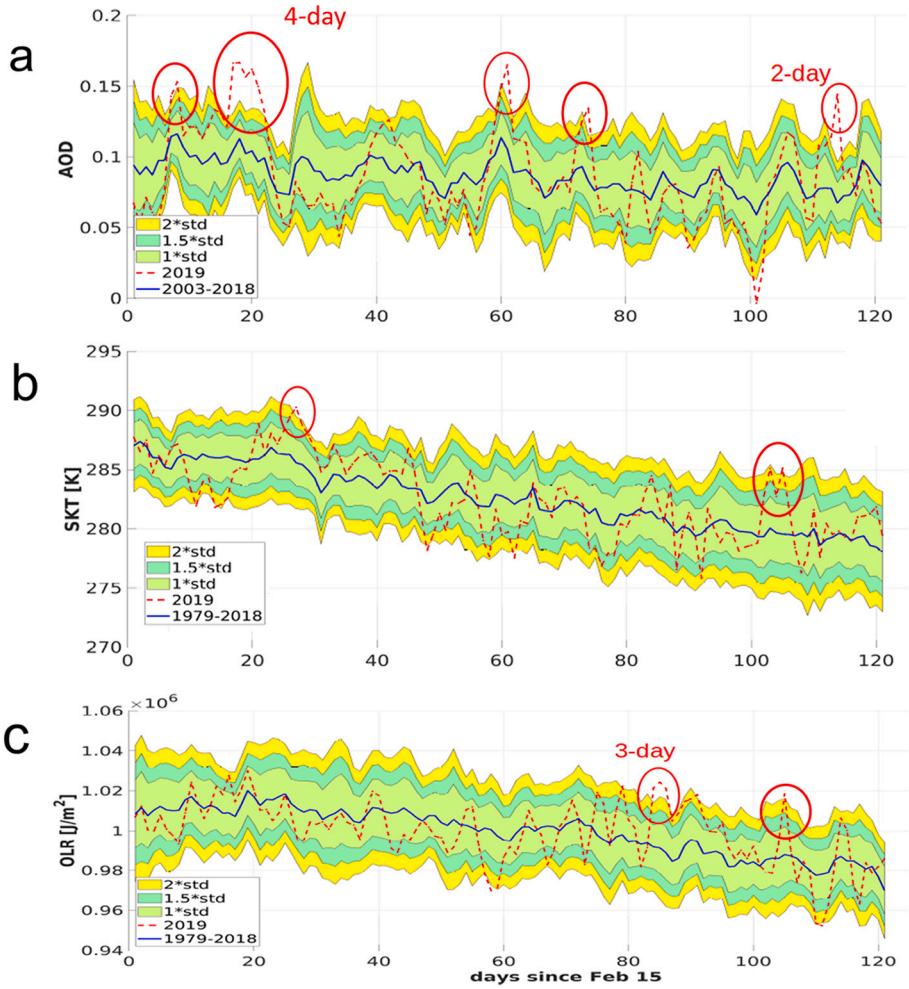

Fig. 4. Case study for the 2019 Kermadec Islands earthquake ECMWF AOD (a), SKT (b) and OLR (c). The 2019 time series (red dashed line) is compared with the historical time series (1979–2018 for SKT and OLR, 2003–2018 for AOD, blue line). The circles put in evidence the identified anomalous days. Coloured stripes indicate 1.0 (green), 1.5 (cyan) and 2.0 (yellow) times the standard deviation (std) from the mean of the historical time series, respectively. The earthquake occurred at the end of the analysed period (120 days). (For interpretation of the references to colour in this figure legend, the reader is referred to the web version of this article.)

the seismic event. If the observable of interest exceeds with a certain persistence the mean of the time series twice the standard deviation, an anomaly is identified. In this work we considered an interval of four months before the earthquake and preferred to identify also single day anomalies, at the cost to have more anomalies than usual.

In particular for ERA5 dataset, that starts from 1979, we focused on physical variables related to thermal radiative interaction of atmosphere with surface, i.e. SKT, TCWV and OLR. ERA5 provides hourly estimates of a large number of atmospheric, land and oceanic climate variables. The data cover the Earth's surface on a 30 km grid and resolve the atmosphere using 137 levels from the surface up to a height of 80 km.

As regard CAMS dataset, content of the main gases, possibly related to surface emissions (Chiodini et al., 2004, 2020), such as CO, SO_2, CH_4 and AOD, have been analysed, with the same 0.25° x 0.25° spatial grid resolution, with the exception of CO dataset that has a spatial resolution with a grid of 0.75° x 0.75°. The CAMS reanalysis dataset covers the period from January 2003 to 2020. We used all data from January 2003 to the date of the earthquake. The CAMS reanalysis is the latest global reanalysis dataset of atmospheric composition (AC) produced by CAMS, consisting of 3-dimensional time-consistent AC fields, including aerosols, chemical species and greenhouse gases (GHGs).

ECMWF climatological analysis for Kermadec Islands 2019 M7.2 seismic event puts in evidence some anomalous days for some of the studied parameters. In particular, AOD shows a 4-day persistent anomaly starting on 3 March 2019, and three single anomalies on 23 February, 17 April and 30 May 2019 (Fig. 4a), with positive anomalies around the epicentre (Fig. 5a). SKT shows two single anomalies on 13 March 2019 and on 30 May 2019 (Fig. 4b), with maximum concentration in northern New Zealand (Fig. 5b). OLR reveals a 3-day persistent anomaly starting on 9 May 2019 and two single anomalies on 15 and 30 May 2019 (Fig. 4c), with the EQ epicentre at the border between maximum and negative values (Fig. 5c). TCWV analysis shows three single anomalies, on 14 March, 31 March and 30 May 2019 (see Supplementary Material). As regards Sulphur dioxide content, it shows two anomalies on 11 April and 3 June (a two-day anomaly) 2019 with spatial concentrations as shown in the Supplementary Material. Methane shows three single anomalies on 10 March 2019, 23 and 25 May 2019, whilst CO analysis does not show any anomaly in the 120 day time window analysed (see Supplementary Material).

A confutation analysis performed for a year without significant

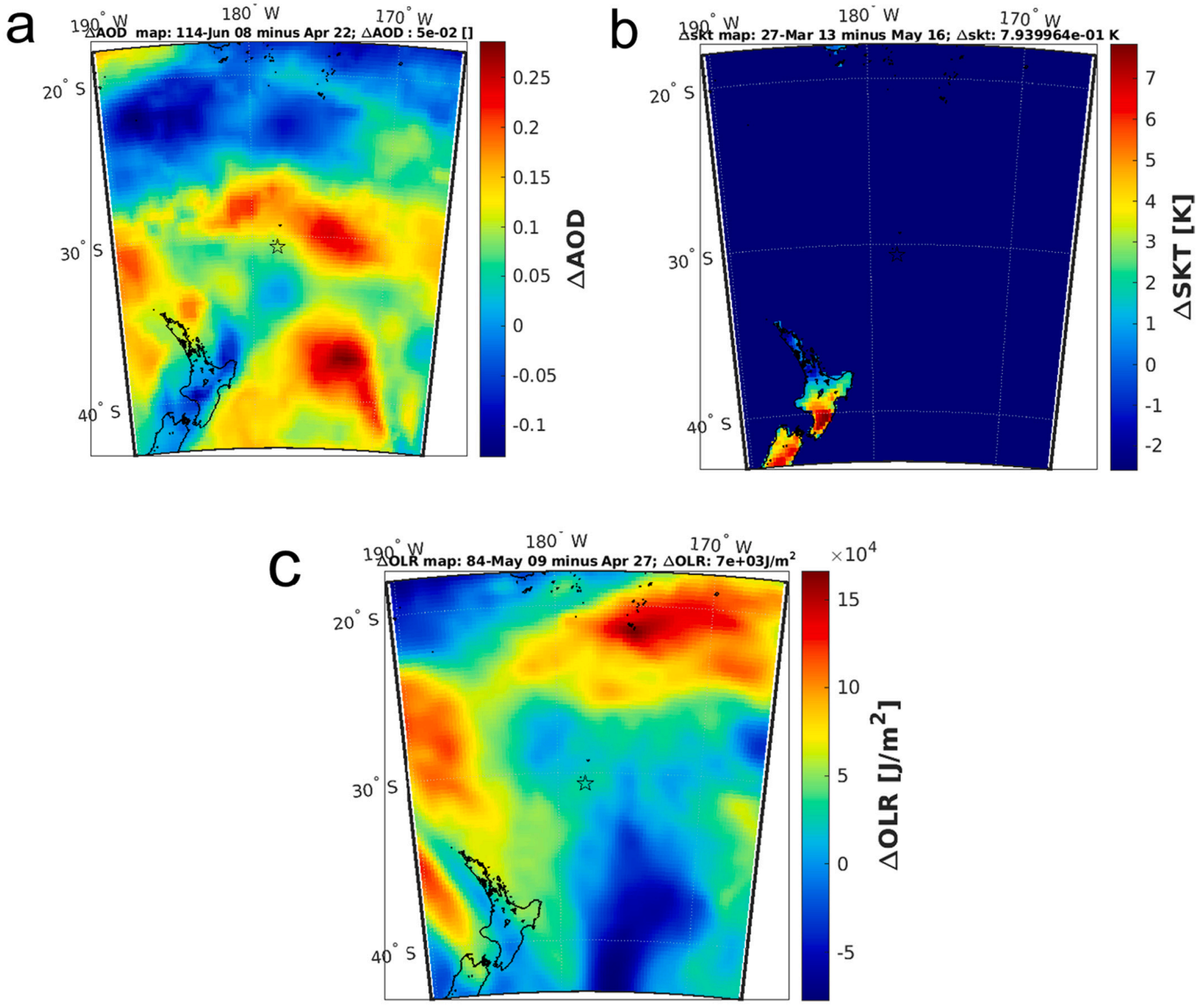

Fig. 5. ECMWF AOD (a), SKT (b) and OLR (c) anomalous day maps of the case study for the 2019 Kermadec Islands earthquake. The values are given as difference with respect to a typical non-anomalous day.

seismicity (i.e. 2018) is shown in the Supplementary Material where SKT and OLR do not show significant anomalies. AOD and SO_2 show many less anomalies than those detected by the same atmospheric quantities in 2019, i.e. the year of the EQ.

3.3. Satellite magnetic and electron density data analysis

After the analyses of lithospheric (i.e. seismological) and atmospheric data, we move to analyse the state of the ionosphere during the preparation of the Kermadec Islands EQ by satellites and GNSS receivers. Swarm and CSES-01 magnetic and Ne datasets are used to analyse and integrate the different approaches that can be implemented to detect electromagnetic anomalies caused by earthquakes preparation phase, thanks to their low earth orbits, at around 500 km of altitude. As shown in the Supplementary Material, starting from MASS (MAgnetic Swarm anomaly detection by Spline analysis; see for example De Santis et al., 2017, 2019b), four different approaches (hereafter also called Method 1, 2, 3 or 4, respectively) have been implemented: 1) classic MASS: using first differences divided by the time interval from sample to next sample and b-splines to remove the long trend; 2) using first differences of the data but removing the long trend by means of a 10-degree polynomial; 3) using the global geomagnetic field model CHAOS (i.e. a magnetic model initially based on **CHA**mp, **Ø**rsted and **S**ac-c satellites; the most recent version 7 also includes Swarm satellite data; Finlay et al., 2020), only for magnetic data, to calculate differences with respect to the satellite data and b-splines to remove the long trend; 4) using CHAOS model to calculate differences with respect to the satellite data and 10-degree polynomial to remove the long trend. The first approach (Method 1), i.e. the classic MASS, has the great advantage to be self-consistent, without the need of a global geomagnetic field model.

The main result of these analyses is a list of the most accurate and consistent anomalies that are provided by the classic MASS, being present in CSES-01 and Swarm magnetic tracks. This study has been performed considering 150 days before the EQ, detecting a promising anomaly 110 days (more than three months) before this event, present in different platform datasets. Fig. 6 shows an example acquired by CSES-01 and Swarm satellites on 25 February 2019. Fig. S11 in the Supplementary Material shows that the solar conditions before and during the found anomaly were quite calm, excluding the possibility of an external magnetic field effect.

In addition, on this day no M5+ EQs have been recorded from the USGS seismic network in a 1500 km area around the M7.2 EQ epicentre, so the anomaly is a great candidate as a possible precursor of the earthquake. From Swarm-CSES-01 joint analysis, the anomaly lasts for several hours from about 9:35 UTC to 17:10 UTC (i.e. 7 h and 35 min), still with a possible residual at 21:15 UTC. The peak of intensity of the anomaly has been recorded by nighttime passage of CSES-01 satellite in the area at 14:35 UTC, reaching a significant anomaly of 20 nT peak-to-peak, which seems in any case too much for a seismo-induced phenomenon.

Fig. 7 shows a CSES-01 anomalous track detected the day before the previous case. Also this anomaly is quite interesting: in fact, the highest intensity is in the Y-East component as expected for internal anomalies (Pinheiro et al., 2011) and it is the only anomaly in the whole track between 50° South and 50° North of geomagnetic latitude. In addition, also this track presents an anomaly intensity in the Y component of about 20 nT. The geomagnetic conditions were quiet (geomagnetic indices: Dst = −1 nT, ap = 4 nT and AE = 24 nT; source: World Data Center for Geomagnetism, Kyoto, http://wdc.kugi.kyoto-u.ac.jp/) and the anomaly is localised over land, in the southern segment of the plate boundary and at the border (but inside) the Dobrovolsky area. It is interesting to notice that the anomalies appear in the magnetic field components (larger in the Y-component) but not in the total intensity: this implies that the perturbation rotates the magnetic field vector without changing its intensity.

Fig. 8 shows a CSES-01 magnetic field track that contains a decrease

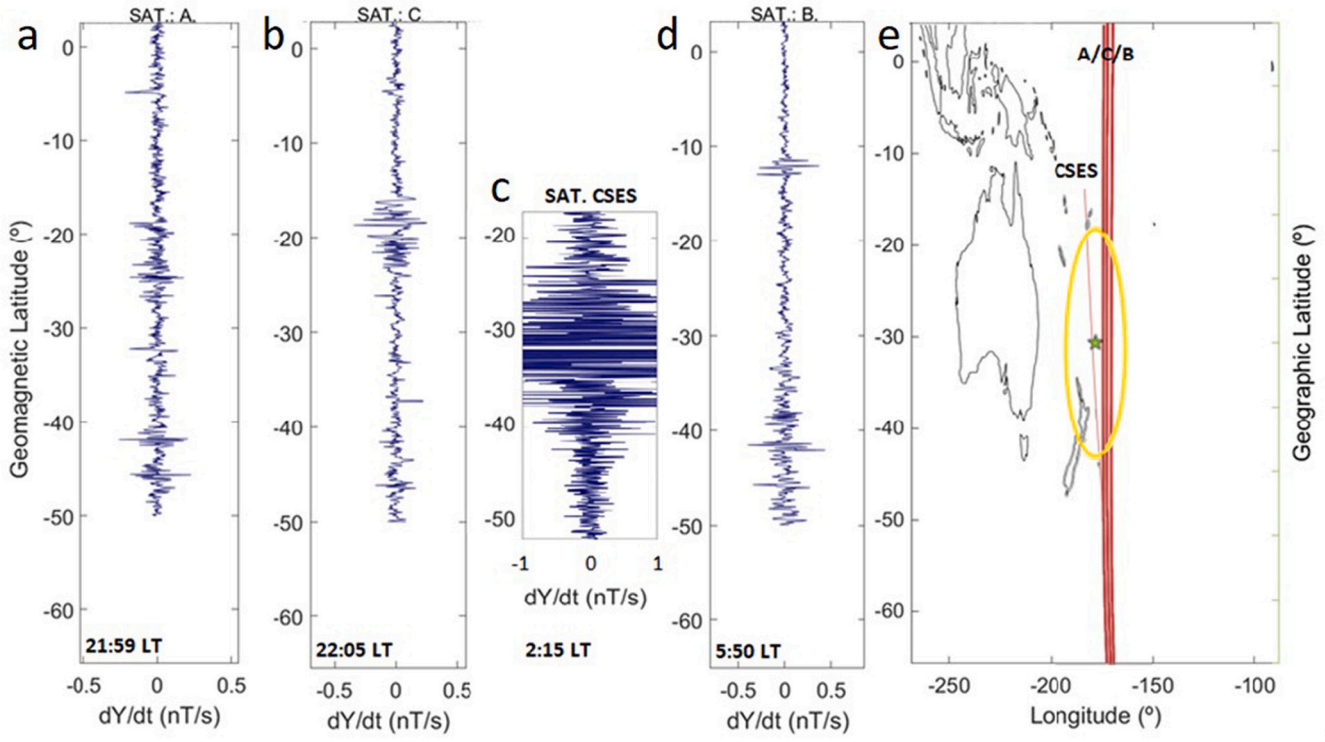

Fig. 6. Magnetic field Y-component analysis using the classic MASS method (Method 1) in different tracks of Swarm A (a), B (b), C(d) and CSES-01 (c) on 25 February 2019 for the local time windows as indicated in the form hh:mm. Red lines in panel e (with the geographical map) correspond to the four satellites' paths. The yellow oval is the Dobrovolsky area; the star is the EQ epicentre. (For interpretation of the references to colour in this figure legend, the reader is referred to the web version of this article.)

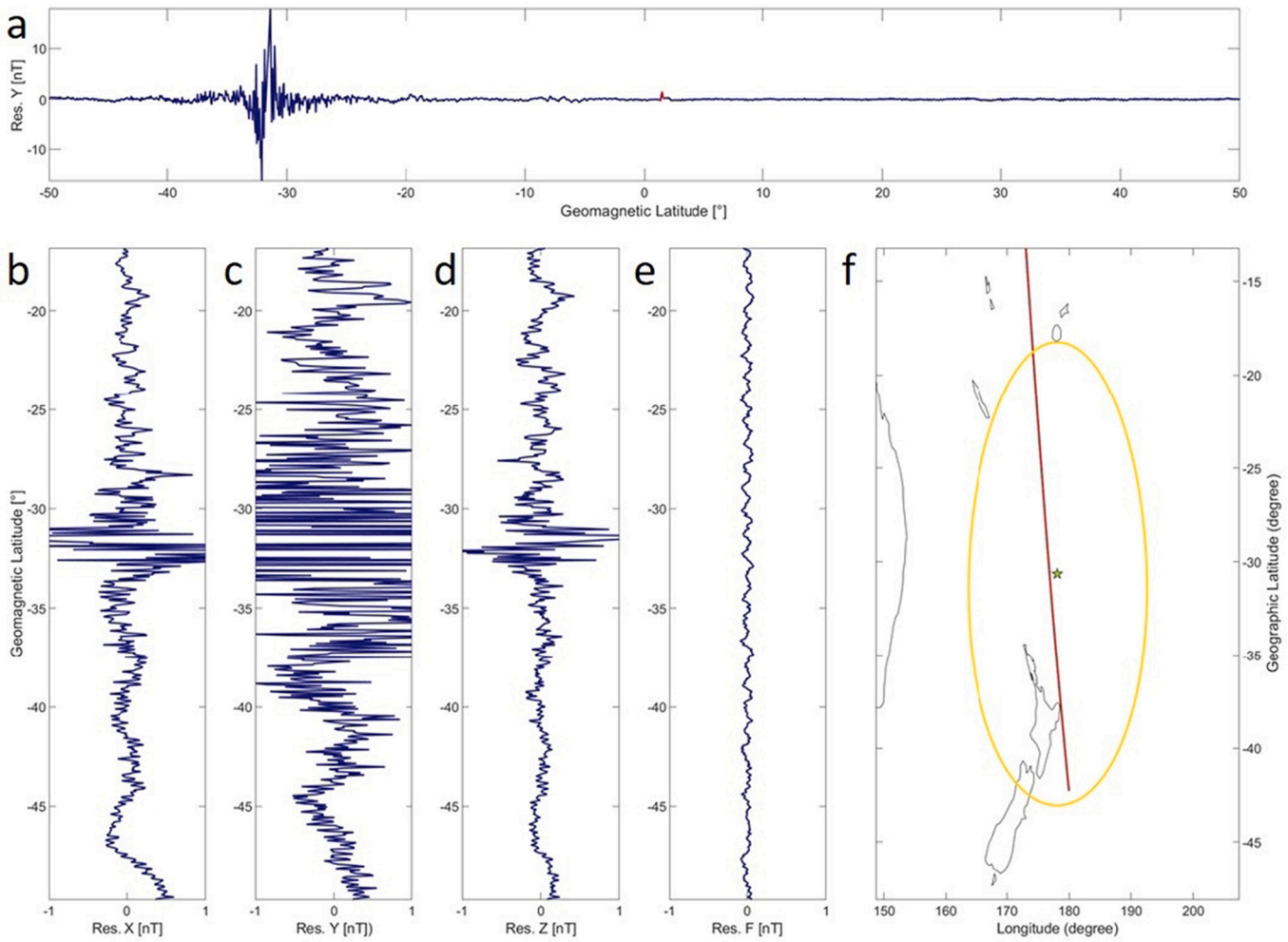

Fig. 7. Anomalous magnetic track of CSES-01 on 24 February 2019 analysed by method 3. a) Residuals of Y component vs. time; Residuals of (b) X, (c)Y, (d) Z and (e) F and (f) geographical map. The yellow oval is the Dobrovolsky area; the star is the EQ epicentre; the red line is the satellite path. (For interpretation of the references to colour in this figure legend, the reader is referred to the web version of this article.)

of Y-East component of magnetic field around the future epicentral latitude (extended a little northern). The track, acquired in geomagnetic quiet time (with Dst = −4 nT, ap = 4 nT and AE = 225 nT), shows a little geomagnetic activity at higher latitudes but the level is not anyway so strong.

Fig. 9 shows the track acquired by Swarm Charlie only 22 h and 36 min before the event. We notice a certain similarity of the anomaly with the track acquired 15 min before the Ridgecrest (California, USA) M7.1 EQ occurrence (see Fig. 1 of Marchetti et al., 2020). In addition, the ionospheric plasma has been investigated, with particular attention to the electron density Ne, to search for possible pre-earthquake ionospheric disturbances by the NeLOG algorithm (see De Santis et al., 2019a, for a full description of the method). NeLOG analyses the decimal logarithm of Ne by a 10-degree polynomial fit (red lines in Fig. 10a) and calculates the residual. If a sample overpasses by k_t times the standard deviation of the residual, it is marked by a blue asterisk in the figure. The method then classifies the track as "anomalous" if it contains >10 anomalous samples in the Dobrovolsky area. Fig. 10 shows an interesting example of an anomalous Ne track of Swarm Alpha satellite acquired 119 days before the M7.2 Kermadec Islands (New Zealand) EQ. This track shows a clear enhancement of Ne at a geomagnetic latitude of about −28° similar to the example shown in De Santis et al., 2021 with CSES-01 satellite in the case of a smaller magnitude earthquake. The track has been acquired during geomagnetic very quiet conditions (Dst = −6 nT and a_p = 0 nT). The same track is given in the Supplementary Material (Fig. S13) where, together with Ne, also the tracks of Te and Vs of Swarm-A satellite are shown.

On 1 June 2019, i.e. two weeks before the mainshock, Swarm Alpha detected an interesting electron density latitudinal profile that crossed the longitude of the incoming earthquake epicentre during nighttime and quiet geomagnetic conditions (see Fig. 11). The red box enlightens a part of the Ne profile that seems to be anomalously increased in terms of its absolute value between −44° and − 29° of latitude. Furthermore the same track shows two perturbations around the mean track value highlighted by continuous and dashed red ovals. Interestingly, all such anomalous features are localised inside the Dobrovolsky area and, in particular, the stronger perturbation, underlined by the continuous red oval, is localised at the same latitude of the future epicentre. Such perturbations not only are unusual at night time LT = 01:13 AM but also are localised southern of the typical geomagnetic latitude of the possible residual of daily EIA that could appear at about −15° / -20° geomagnetic latitude, and also sufficiently far from the South pole. Therefore for exclusion the remaining hypothesis on its origin could be a seismo-induced phenomenon.

3.4. Total Electron Content (TEC) data analysis

TEC data from GNSS receivers can also be analysed to detect electromagnetic anomalies possibly related to impending earthquakes. Vertical TEC (vTEC) data calibrated applying the techniques described

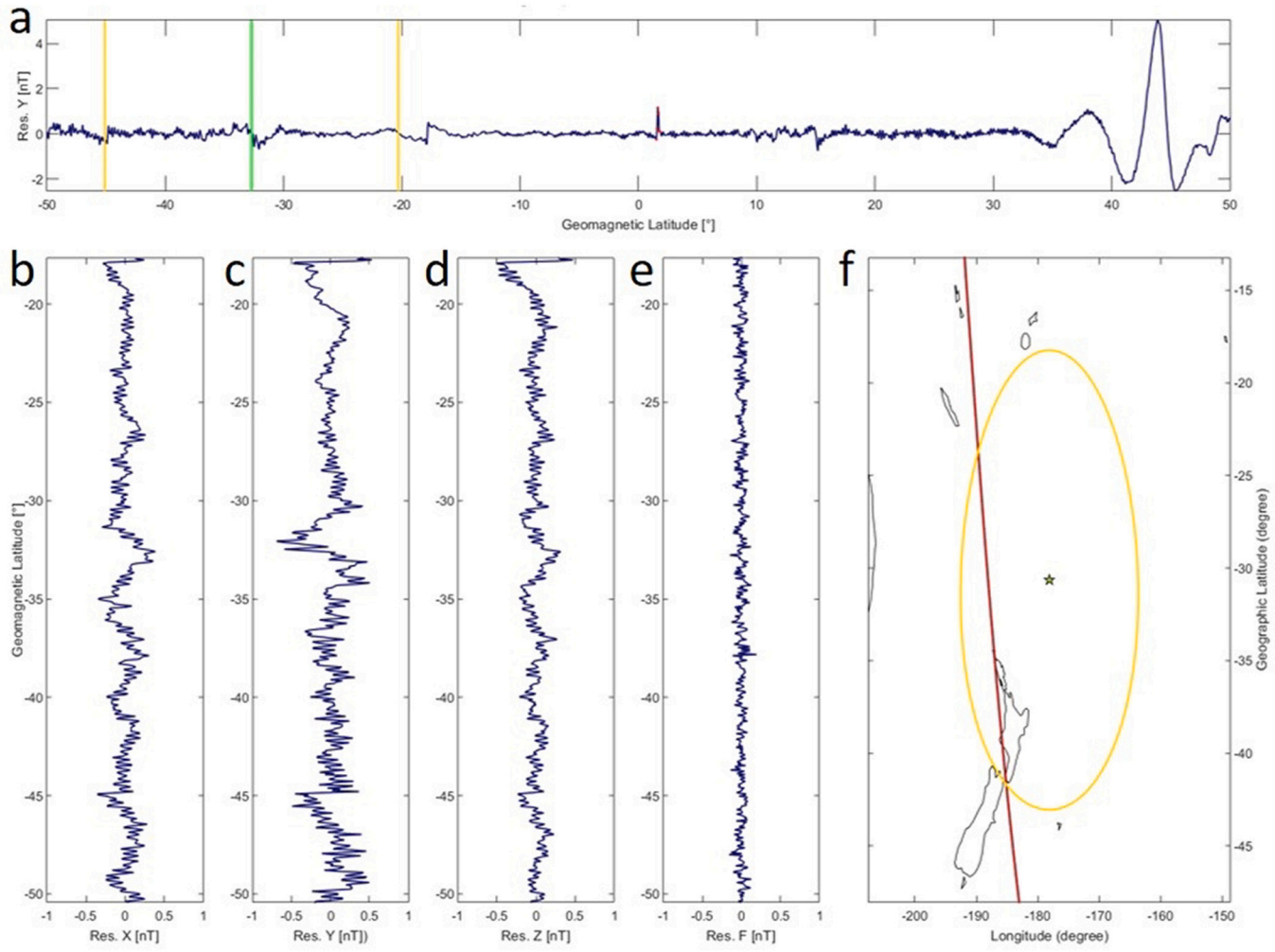

Fig. 8. As Fig. 7 but on 30 April 2019 analysed by method 3. In (a), the vertical lines represent epicentral latitude (green) and limits of the Dobrovolsky area (yellow). In (f), the green star represents the epicentre location while the yellow circle is the corresponding Dobrovolsky area. (For interpretation of the references to colour in this figure legend, the reader is referred to the web version of this article.)

in Ciraolo et al. (2007) and Cesaroni et al. (2015) to RINEX data recorded from 4 months preceding up to 1 month after the earthquake occurrence at selected stations of the GeoNet GNSS/GPS network are used for this purpose, i.e. RAUL, GLKZ and PYGR (see Fig. 1b).

Anomalous variations of vTEC are defined following four different approaches, respectively applied to a single station (method **1**, applied to data close to the epicentre), two stations (methods **2** and **3**, consisting of differential analyses between data close to the epicentre and rather distant ones), and three stations (method **4**, differential analysis among data from stations at different distances from the epicentre). For all the methods, geomagnetic conditions are taken into account in order to exclude anomalies of external origin.

Among such approaches, the two-station differential analysis of method **3** seems to be the most promising, and is presented here in detail (for the detailed definitions and analyses by the other methods, see the Supplementary Material). In this method, the vTEC relative deviations (dTEC) between data of a couple of distant receivers is considered, in the specific:

$$\mathrm{dTEC} = (\mathrm{vTEC}_{\mathrm{RAUL}} - \mathrm{vTEC}_{\mathrm{PYGR}})/\mathrm{vTEC}_{\mathrm{PYGR}}, \quad (5)$$

being RAUL receiver (29.24° S; 177.93° W) the closest available to the earthquake epicentre, with a distance of 156 km, while PYGR (46.17° S; 166.68° E) is the most distant one among those of the GeoNet network, with a distance of about 2170 km (Fig. 1b). This means that dTEC large values reflect vTEC large values near the epicentre in correspondence to lower values outside the earthquake preparation zone, being then considered possibly affected by pre-earthquake processes.

In method **3**, the anomalies are defined by comparing the dTEC values calculated every 30 s to the mean linear trend m of the linear fit to data within the 4 months prior to the earthquake. In this case, an anomaly is defined as a set of dTEC values continuously exceeding $m + 2$ TECU (corresponding to about $m + 3.5\sigma$ in case of a Gaussian distribution of the residuals) for at least 5 min. The anomalies occurred under disturbed geomagnetic conditions are discarded, where $|\mathrm{Dst}| > 20$nT or AE $>$ 200 nT conditions are applied to the instantaneous and daily maxima of the corresponding geomagnetic indices as a proxy of disturbed conditions. Fig. 12 shows the application of this method to the earthquake under analysis. In the same figure also the EQ occurrences are shown together with their range of magnitudes (when more than one EQ occurred on the same day and in the Dobrovolsky area).

This analysis revealed three possible precursory anomalies, some of which were detected also using different approaches. In particular, the 18 March anomaly is recognized also by method **2** (Fig. S16 in the Supplementary Material), and the one of 5 June by both methods **1** applied to RAUL data (Fig. S15) and method **2**, despite the latter confirming the anomaly only with respect to the first background (Fig. S16a). It should be noted here that the application of method **4** for the three-station differential analysis revealed only an anomaly on 18 March, detected also by both the methods for the two-station differential

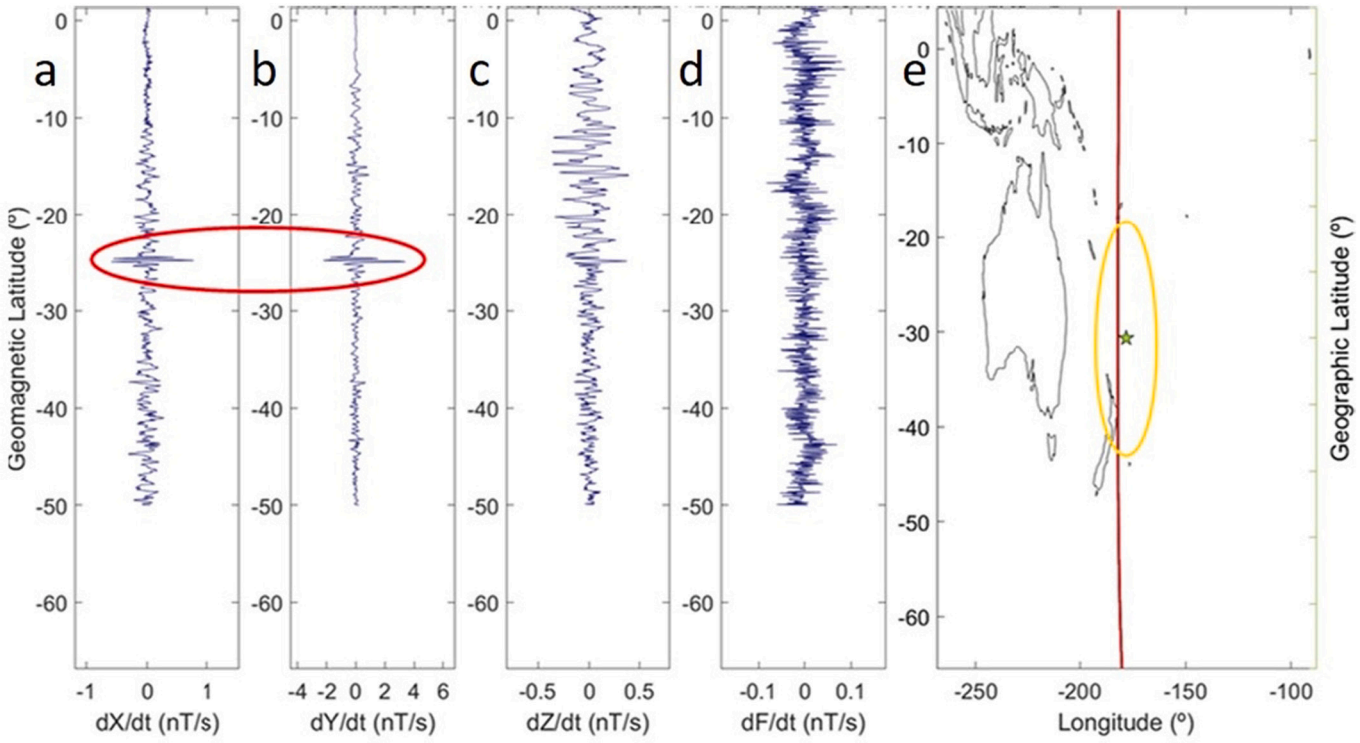

Fig. 9. Anomalous magnetic track of Swarm Charlie on 15 June 2019 (the day of the earthquake) analysed by method 1 (MASS), showing the first differences of a) X, b) Y, c) Z magnetic field components and d) total intensity; e) geographical map with Dobrovolsky area (yellow), satellite orbit (red) and epicentre (green star). (For interpretation of the references to colour in this figure legend, the reader is referred to the web version of this article.)

analysis, as possibly related to the impending earthquake. Of course, we cannot exclude that some anomaly could be associated to a closer EQ with lower magnitude (indicated by a vertical green arrow in Fig. 12), but since the discrimination is impossible, we attribute all found anomalies to the preparation of the largest magnitude M7.2 EQ of interest.

The Supplementary Material also presents the same analysis but applied to the same 4-month period of the 2018 year as confutation analysis. Please note that this tectonic area is very active seismically so it is almost impossible to find periods without significant seismicity: we chose 2018 because only two M5.7+ EQs (actually one outside but close to the period of interest) occurred in this period (while in the investigated 2019 year there were 9 EQs). Also in 2018 there are some anomalies, but many less than in 2019, and those occurred could be precursors of the few EQs occurred in this period of 2018.

3.5. CSES-01 Search Coil Magnetometer and Electric Field Detector spectral analysis

Spectral analysis of magnetic and electric signals acquired by Search Coil Magnetometer (SCM) and Electric Field Detector (EFD), working on board CSES-01 satellite (Wang et al., 2018), were also considered in the period 1 June - 13 July 2019. In particular, we analysed magnetic and electric field variations in the Extremely Low Frequency band (ELF, 200–2200 Hz, with 10.24 kHz and 5.12 KHz sampling rate, respectively). Our aim is to detect anomalies preceding large earthquakes, by means of the evaluation of the spectral information content emerging in some frequency band, in similar way as applied in previous case studies (e.g. Carbone et al., 2021; Piersanti et al., 2020; Wang et al., 2018). Fig. 13 shows the CSES-01 orbit 74,991 (day 10 June 2019), passing through the Dobrovolsky area (green circle) of the Kermadec Islands (New Zealand) EQ, while Fig. 14 illustrates the spectrograms of both SCM (a) and EFD (b) in the ELF band.

Observing the spectrograms of the magnetic field (all three components) and the electric field (mainly Y and Z components), we can see the presence of a possible anomaly within the Dobrovolsky area at frequencies lower than around 500 Hz (see Fig. 14).

To better study this anomaly, we resorted to the concept of Shannon Entropy (Shannon, 1948). A spectrogram represents the temporal variation of the power spectral density; starting from this, at any moment the entropy H(S) associated with the spectrum S is calculated as defined by Shannon (1948):

$$H(S) = -\sum_{i=1}^{N} p(s_i) \cdot log_{10} p(s_i) \quad (6)$$

where S is a discrete random variable that can assume N distinct values $s_1, \ldots, s_N$ and the probability function $p(s_i)$ represents its statistical distribution. The results are shown in the Fig. 15, which represents the trends of the normalised entropy $H(S)/log_{10}N$ as time varies, for the magnetic and the electric fields. Entropy is higher if there is decorrelation between samples, while it is lower when values $s_1, \ldots, s_N$ are correlated.

As you can see, in the area near the epicentre there seems to show a clear correlation between the samples of the spectrum of magnetic and electric fields, while elsewhere these seem to be less correlated with each other.

The main feature that emerges from both the magnetic and electric field spectrograms (Fig. 14) is the power concentration around the Dobrovolsky area (green vertical lines) in a limited region of the spectrum (below and close to 500 Hz). A similar anomaly frequency was detected for 2009 L'Aquila EQ (in that case it was 330 Hz; Bertello et al., 2018). The energy concentration in a limited range of frequencies reflects in the evident concave behaviour in the entropy (Fig. 15). A deeper inspection reveals the same power concentration in the equivalent spectral band ($f \leq 500$ Hz) in both magnetic and electric field spectra, in a portion of the orbit (latitude interval) which is the symmetrical counterpart with respect to the magnetic equator (see Fig. 13). Although less energetic (and so less clear), of course this similar feature emerges,

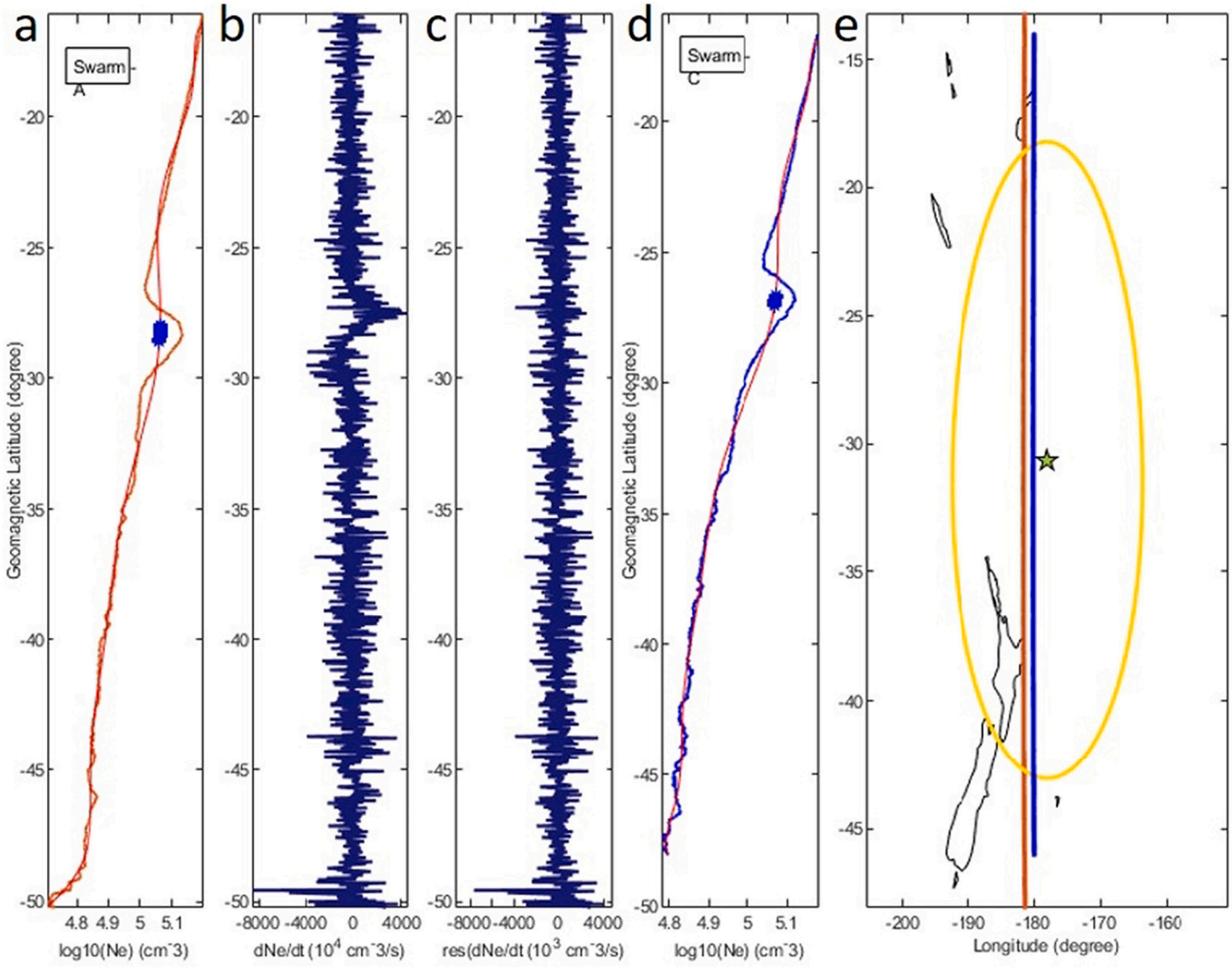

Fig. 10. Anomalous electron density Ne track of Swarm Alpha on 16 February 2019 (~119 days before the mainshock) elaborated by NeLOG with $k_t = 2.5$. From left the figure shows: a) the log Ne, b) the first differences of Ne and c) residual with respect to the mean polynomial trend for satellite Alpha; then it shows d) the log Ne for Swarm Charlie. The two orbits are shown in the geographic map in e): red for Alpha and blue for Charlie. (For interpretation of the references to colour in this figure legend, the reader is referred to the web version of this article.)

correspondingly, in their entropies, where the evident depression around the Dobrovolsky area replicates to a lesser extent in the symmetric area, delimited by the magenta vertical lines (Fig. 15). A clear and founded explanation requires a deeper and focused inspection. Nonetheless, a simple speculation could be that the entropy decreases over the preparation area (represented by the Dobrovolsky region) because of the coupling between the lithosphere under stress and the above ionosphere (through the atmosphere in the between); and that coupling reflects to the symmetric latitudes through the current system along the magnetic field lines (e.g. Sorokin et al., 2019).

4. A comparison with 2019 M7.1 Ridgecrest Earthquake

In this section, the occurrences of the various precursors of the Kermadec Islands EQ with those of Ridgecrest EQ (occurred on 6 July 2019 03:19:53 (UTC) - 35.770°N 117.599° W, 8.0km depth) are compared. The likeness of the pre-earthquake anomalies between the two earthquakes is instructive because the two earthquakes have similar magnitudes, although they occurred in two very different tectonic contexts. Table 1 summarises the occurrences of the anomalies, where the number corresponds to the day with respect to the EQ occurrence, being in bold black those of Kermadec Islands EQ and in light black those of Ridgecrest EQ. The rows of the table are placed from top to bottom almost in altitude order, i.e. from lithosphere, atmosphere to ionosphere. In general, the anomalies tend to occur closer to the earthquake occurrence going up into the atmosphere and ionosphere. As shown by Table 1, the lithospheric anomalies (either in terms of *b*-value decrease and the beginning of the R-AMR acceleration) precede all the atmospheric and ionospheric anomalies. In addition, some atmospheric and ionospheric anomalies appear at almost the same time with respect to the EQ occurrence: impressive almost simultaneous precursors (within a 10-day interval) appear around 90 days before the EQ for aerosol (AOD and AOT), SKT, TCWV and TEC values. Interestingly, the final acceleration (increasing number of anomalies) occurs as the earthquake is approaching (say, in the last two weeks), especially in the ionosphere. Another consideration is speculative, trying to connect atmospheric to ionospheric anomalies: while some of the latter (here called **Case 1** ionospheric anomalies) occur well before the atmospheric anomalies (e.g. Y and Ne at >100 days), others (here called ***Case 2*** ionospheric anomalies) seem to occur with some delay (5–10 days) with respect to the atmospheric anomalies. This delay seems more typical of a diffusion propagation of the atmosphere-ionosphere coupling that requires a

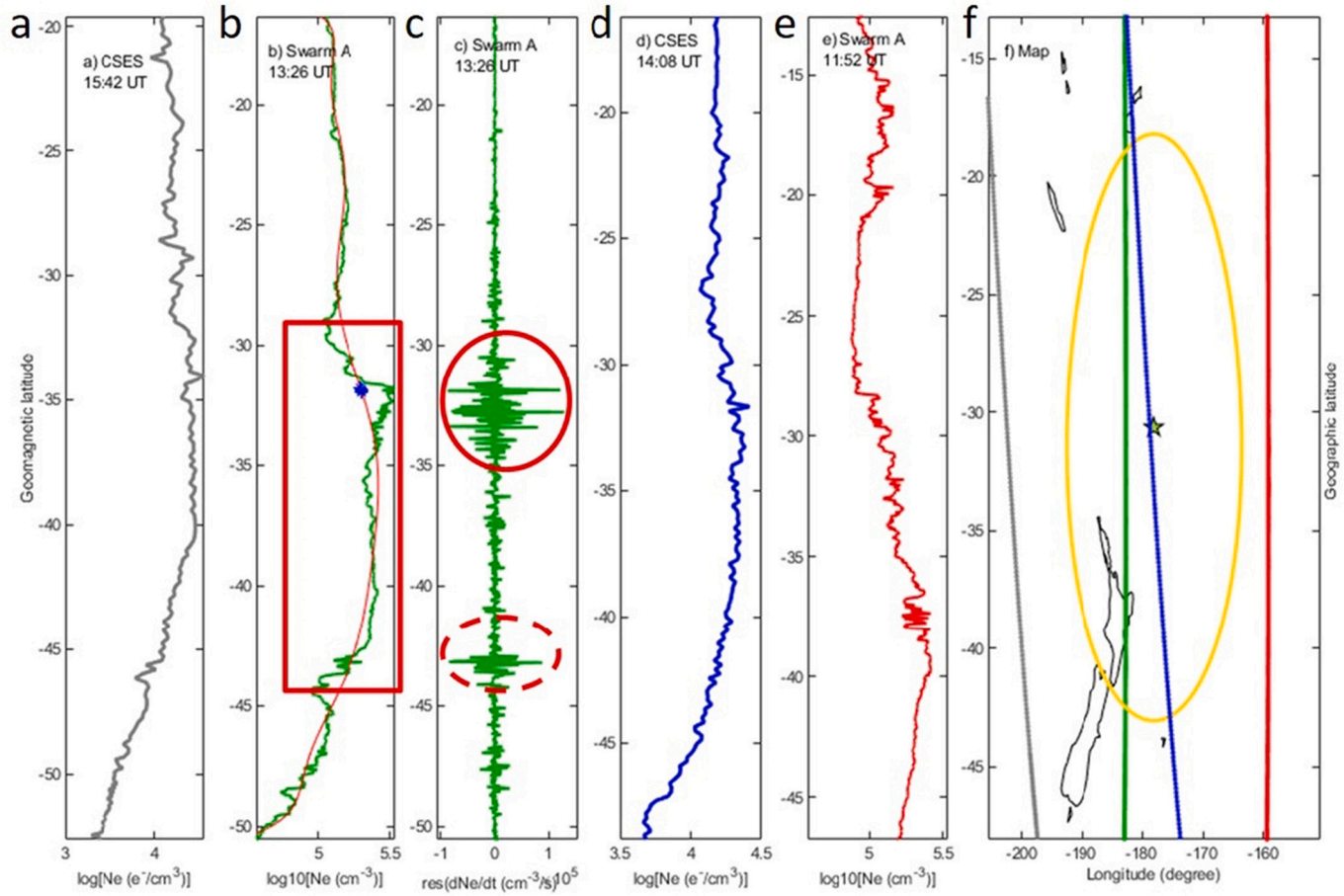

Fig. 11. CSES-01 and Swarm Alpha electron density tracks acquired on 1 June 2019 (~2 weeks before the mainshock). a) CSES-01 acquired at 15:42 UT; b) Swarm Alpha acquired at 13:26 UT; c) residual analysis by NeLog of track shown in b; d) CSES-01 track acquired at 14:08 UT; e) Swarm A acquired at 11:52 UT; f) map with the ground projections of the satellite tracks with the same colour used in the previous panels.

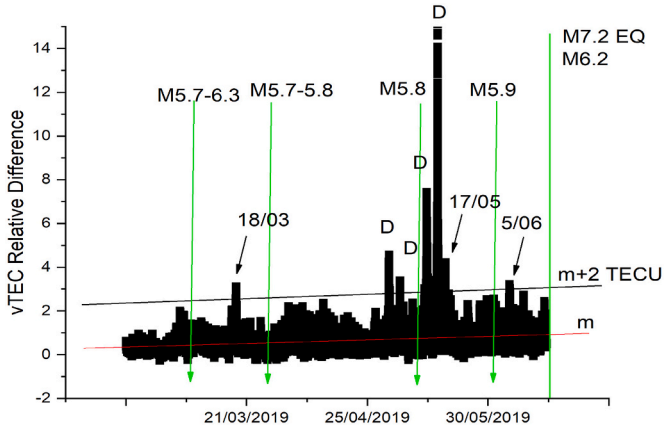

Fig. 12. vTEC two-station differential analysis (method **3**) for the 2019 M7.2 Kermadec Islands EQ. The black arrows indicate three anomalous days, while the vertical green line represents the time of the mainshock occurrence. D stands for disturbed ionosphere. In this figure, m is the mean trend (red line), and m + 2 (black line) is the chosen upper threshold for anomalies identification. The vertical green arrows represent the M5.7+ EQs occurred in the period of investigation (also the range of EQ magnitudes is shown). Please note that, on the same day of the M7.2 mainshock, another EQ occurred with magnitude 6.2.

mean vertical velocity of the order of 50–100 km/day and that produces the Case 2 anomalies in the ionosphere. The Case 1 anomalies in the ionosphere could be generated by a direct electromagnetic coupling between the lithosphere and the ionosphere, e.g. through the p-holes (Freund, 2011).

5. Discussion and conclusions

A full multiparametric and multilayer investigation of the case study of the M7.2 Kermadec Islands (New Zealand) 2019 EQ has been presented here. A chain of processes that start from the lithosphere and propagate through the atmosphere and finally reach the ionosphere is found through Table 1. In particular, we have analysed seismological, atmospheric, satellite and ground electromagnetic data to study the potential LAIC phenomena. The seismological data analysis showed that an acceleration took place during the preparation phase of the earthquake and the R-AMR technique predicted the magnitude of the impending EQ. From atmospheric data, several anomalies before the earthquake have been retrieved: AOD anomaly appears first around 100 days before the EQ, then followed by CH_4, SKT and TCWV around 90–80 days before the EQ. SO_2 anomaly appears around 60 days before the earthquake, almost together with another AOD anomaly. Among all atmospheric quantities, OLR is the last, appearing around 30–40 days before EQ. Finally SKT, TCWV and OLR show other anomalies around 15 days before EQ. Then 6 days before EQ, another AOD anomaly appears. The starting sequence of the anomalies resembles that found for two large Chinese earthquakes, i.e. 2008 M8 Wenchuan EQ and 2013 M7 Lushan EQ (Liu et al., 2020a), where AOD appeared >80 days before

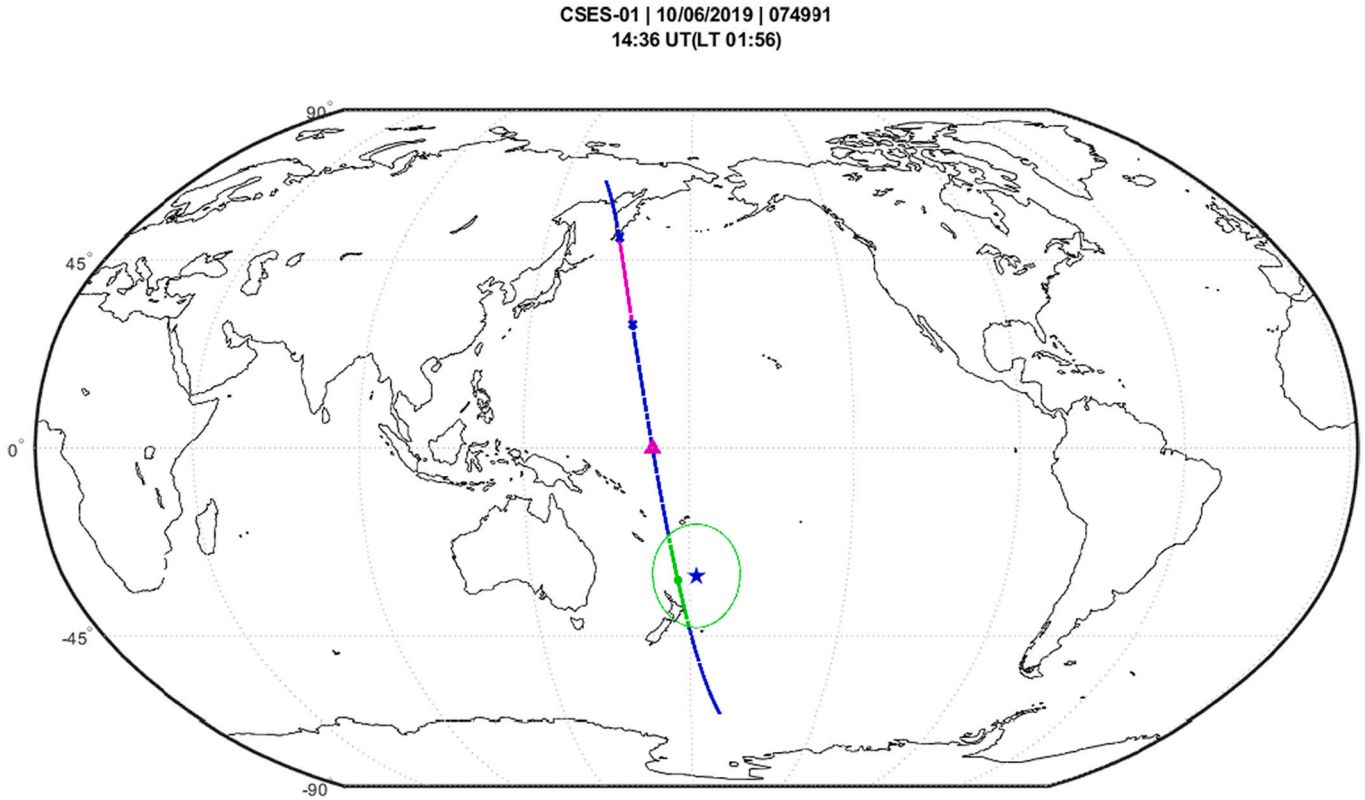

Fig. 13. Map showing the epicentre (blue star) of 2019 Kermadec Islands EQ, the corresponding Dobrovolsky area (green circle) and the track of the orbit number 74991 of CSES-01 (blue line). The green segment of the orbit inside the Dobrovolsky area corresponds to the interval within the solid green vertical lines in the spectrogram (Fig. 14); the magenta section in the upper part is its symmetric (with respect to the magnetic equator) counterpart. The small magenta triangle along the orbit represents the direction of the satellite fly (i.e. it is an ascending orbit). (For interpretation of the references to colour in this figure legend, the reader is referred to the web version of this article.)

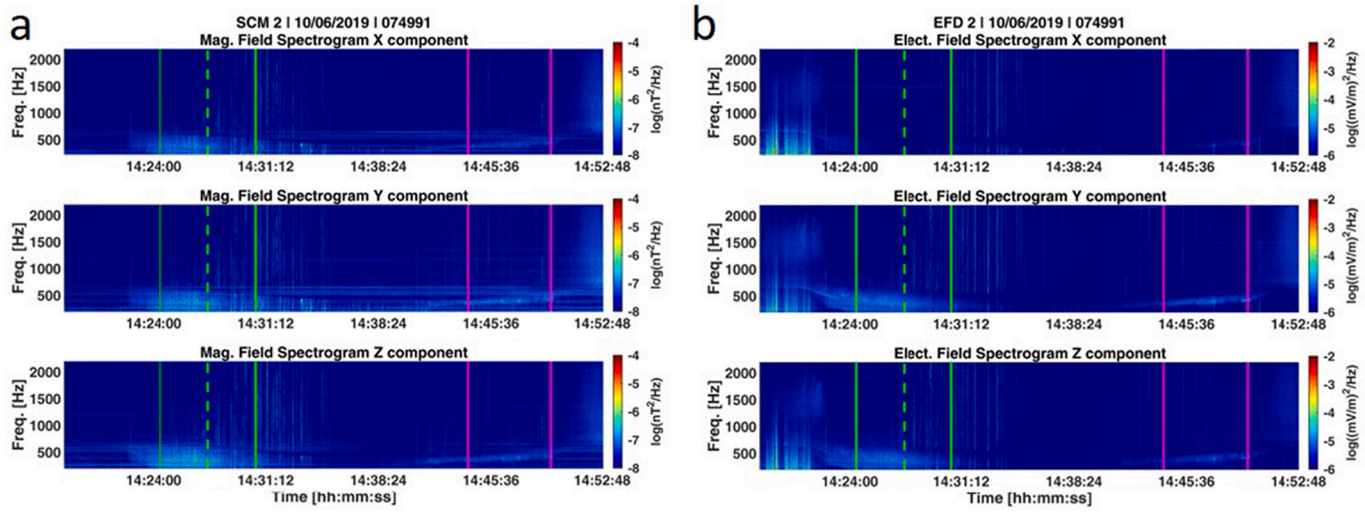

Fig. 14. Spectrograms of magnetic (a) and electric (b) field in the ELF band 5 days before the 2019 Kermadec Islands EQ (orbit number 74991). The solid green vertical lines correspond to the limits of the Dobrovolsky area; the dashed line indicates the time of the minimum distance between the epicentre and the orbit, while the area delimited by the magenta vertical lines represents the symmetric counterpart with respect to the magnetic equator. The intermittent noise of EFD at lower latitudes (well before 14:24:00) is very different from that within the Dobrovolsky region and probably due to some geomagnetic activity at the Auroral region. (For interpretation of the references to colour in this figure legend, the reader is referred to the web version of this article.)

EQ, preceding TCWV and SKT. The increase of aerosols before large earthquakes was already recognized >40 years ago (Tributsch, 1978) and confirmed in many subsequent works (e.g. Liperovsky et al., 2005; Liu et al., 2020a, 2020b). The appearance of a thermal anomaly at 90, 72, 25 and 15 days before the earthquakes of Ridgecrest or Kermadec Islands, shows that temperature is another important atmospheric precursor. Qin et al. (2012) analysed the temperature changes (in terms of air surface temperature and surface latent heat flux, SLHF) on occasion of two important 2010–2011 earthquakes in New Zealand (therefore in a region just a little more southern than the area of the present studied

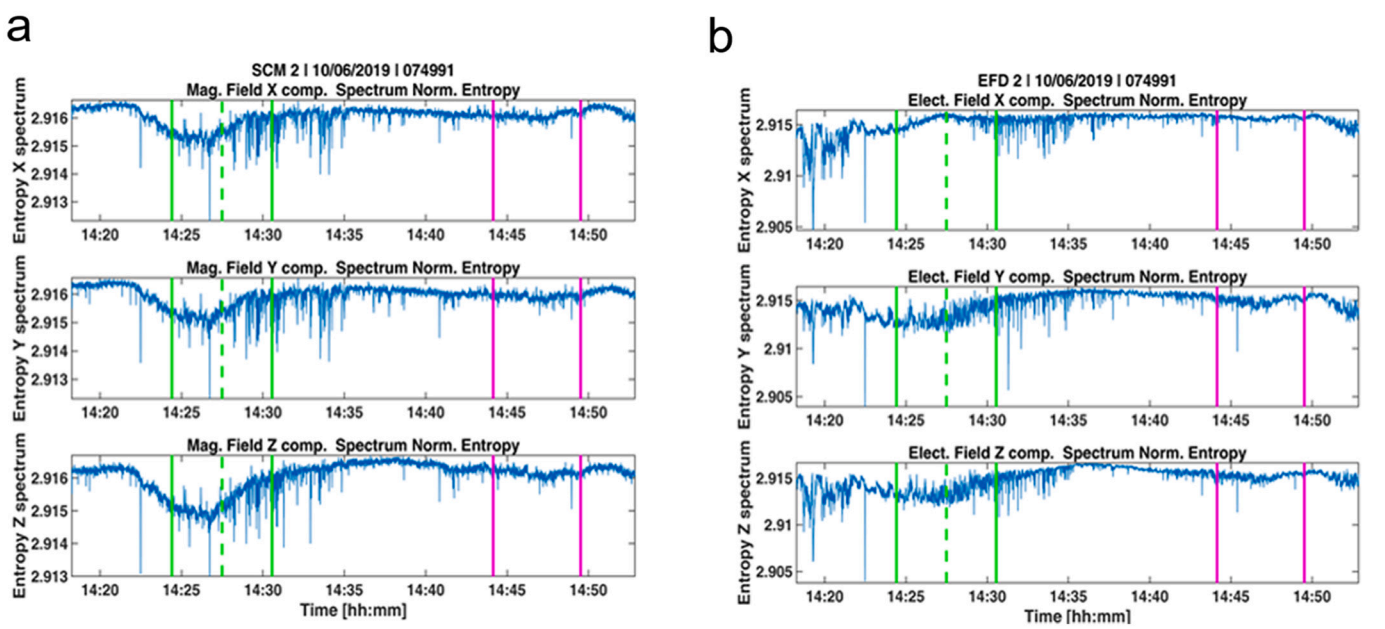

Fig. 15. Normalised entropy of power spectral densities of X,Y,and Z components of magnetic (a) and electric field (b) in the ELF band 5 days before the 2019 Kermadec Islands EQ (orbit number 74991). The solid green vertical lines correspond to the limits of the Dobrovolsky area; the dashed line indicates the time of the minimum distance between the epicentre and the orbit, while the area delimited by the magenta vertical lines represents the symmetric counterpart with respect to the magnetic equator. The large variability at the beginning of the electric field signal corresponds to perturbation at higher latitudes, so it is not related to pre-earthquake phenomena. (For interpretation of the references to colour in this figure legend, the reader is referred to the web version of this article.)

Table 1
Multi-precursor anomalies and their occurrence in terms of the day to the earthquake (Kermadec Islands EQ anomalies in bold black, Ridgecrest EQ anomalies in light black).

	Days to EQ	> 120	120	99	89	79	69	59	49	39	29	19	9
	from		-	-	-	-	-	-	-	-	-	-	-
	-		100	90	80	70	60	50	40	30	20	10	0
	to												
	b-value	**290**											
Lithosphere	R-AMR	**180**											
	D			90		75	65,60						
	AOD						**59**						
	AOT		**100–103**				60						**6**
	SKT			**93**									
				90		75					25	**15**	
Atmosphere	TCWV			**92**	85	**75**						**15**	
	CH_4			**99**		70					**20–22**		
	SO_2						**66**					**12**	
	OLR									**36, 30**		**15**	
	Ionosonde									34			
	IONO1												7
Ionosphere	TEC				**89**						**29**	**10**	
	ELF												**5**
	Y		**110**				65–70						**1**
	Ne		**109–119**										

Bold Black: Kermadec Islands (NZ) M7.2 EQ (this article).
Light Black**:** Ridgecrest (USA) M7.1 EQ.
D > 0 strength parameter Ridgecrest EQ – incremental part of the stresses (Bondur et al., 2020).
SKT, TCWV, CH_4, AOT, Ionosonde, Swarm Y mag. field (De Santis et al., 2020).
IONO1 - Ionospheric variability – Ridgecrest EQ (Pulinets et al., 2021).

earthquake) and noticed that there were some series of thermal anomalies at about 30 days before the mainshock (3 Sept. 2010 M7.1) and 60 and 3–4 days before the largest aftershock (21 February 2011 M6.3). Qin et al. (2012) also proposed four possible different mechanisms of Lithosphere- (Coversphere)-Atmosphere coupling: magmatic-hydrothermal fluids upwelling, soil moisture increasing, underground pore gases leaking, and positive holes activating and recombining.

Magnetic field and electron density data analyses from Swarm and CSES-01 satellites detected some interesting anomalies. In particular, a magnetic anomaly has been detected on 25 February 2019 during nighttime: comparing the different satellites (Swarm and CSES-01) that crossed the same region at different times, it was possible to follow the temporal evolution of the anomaly. In addition, not shown here, a clear increase of electron density was identified on the night of 26 February 2019, noticing that the maximum Ne value was very close to the future epicentre of the earthquake, and the solar conditions were relatively quiet (see Supplementary Material). Thanks to the orbital sun-synchronous configuration of CSES-01 (precisely at the same

nighttime or daytime), it was possible to confirm that Ne was incremented during deep nighttime, by reducing the chances that it could be just a residual of the daily activity. Furthermore, it was possible to confirm the consistency of Ne latitudinal profiles between CSES-01 and Swarm satellite missions. Another satellite payload analysed here was the Electric Field Detector on board CSES-01 satellite. An anomaly within the Dobrovolsky area, more evident in Y and Z components and similar to what was already detected in the spectrograms of the magnetic field from Search Coil Magnetometer was observed. Finally, from ground GNSS data analysis we have considered TEC data and identified three possible precursory anomalies, some of which were detected also using different approaches, from around 90, 30 and 10 days before the earthquake.

Preliminary conclusions show the necessity of integrating multiple datasets to better understand the preparation phase of medium-large earthquakes. Furthermore, the importance of the CSES-01 satellite, in conjunction with the Swarm satellites, has been shown in several contexts, not only useful to better constrain the state of the ionosphere, but also to find several disturbances possibly related to the earthquake occurrence. It has been seen that some of these characteristics have also been detected by the Swarm three-satellite constellation, proving the good integration between both satellite datasets and the potential of the methodology applied.

From the obtained results, summarised by Table 1, two kinds of LAIC can be found: one is practically direct, so its nature should be electromagnetic, as due to the release of p-holes and their propagation up to the ionosphere. The other is more typical of a thermodynamic diffusion process, probably due to a change of temperature and humidity that starts at the ground-atmosphere interface and slowly propagates through the atmosphere up to the ionosphere. A comprehensive way to collect all data anomalies is plotting the cumulative number of all anomalies for Kermadec Islands EQ with time (Fig. 16). A power law as given by eq. (1) fits very well the data pointing to the time of EQ occurrence. This agrees with the analogous power law behaviour of the cumulative number of anomalies for Ridgecrest EQ (De Santis et al., 2020), as approaching to the EQ occurrence. We point out that a power-law behaviour in time is typical of critical systems approaching a critical point where there is a significant change of the system properties (e.g. De Santis et al., 2019c). In this scenario, the EQ is a critical point of the lithosphere, and its imminent occurrence leaves some clues also in the atmosphere and ionosphere, because of their coupling with the lithosphere during the EQ preparation phase.

The results we found in this work were not obtained by chance: the Supplementary Material shows also a confutation analysis, either considering a random simulation or another year (i.e. 2018) without significant seismicity. In the former case, as expected the cumulative number of anomalies does not resemble a power law but a linear trend; in the latter case, when applied to the atmospheric and TEC data analyses, the anomalies are almost absent or just a few, i.e. many less than those found in the year of the earthquake.

The present results confirm those of previous case studies, such as the 2015 Mw7.8 Nepal EQ (De Santis et al., 2017), the 2016 Mw7.8 Ecuador EQ (Akhoondzadeh et al., 2018), the 2017 Mw7.3 Iran-Iraq border EQ (Akhoondzadeh et al., 2019), the 2018 Mw7.5 Indonesia EQ (Marchetti et al., 2019) and the 2019 Mw7.1 Ridgecrest California EQ (De Santis et al., 2020).

In the future perspective, we would like to extend this multi-parametric and multi-layer approach to new case studies, especially occurring during the Swarm and CSES-01 data simultaneous availability. We plan to present full multiparametric and multilayer investigations also of other large earthquakes with comparable magnitude. For instance, we could also extend the analysis to more recent cases, such as M7.1 Japan and the two concomitant events of 21 May 2021 in China (Madou Mw7.3 and Yangbi Mw6.1). Moreover, the intercomparison of all new and old results will allow us to confirm the chain of anomaly occurrences of different parameters and then validate the best LAIC model.

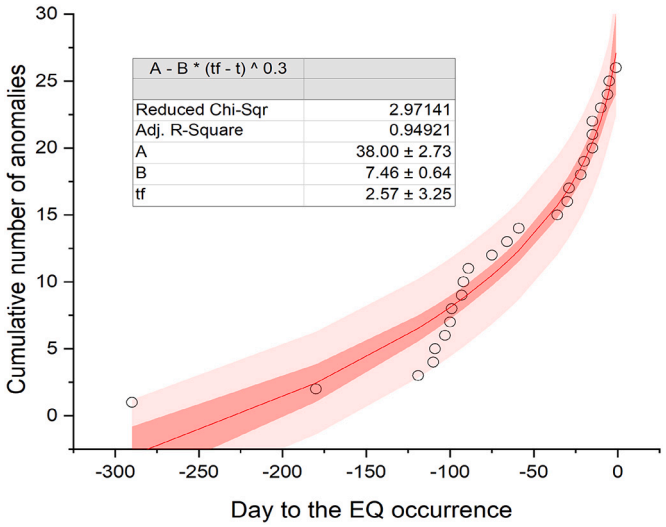

Fig. 16. Cumulative number of the anomalies found for Kermadec Islands EQ vs. time: the best fit (bold red curve) is a power law similar to eq. (1) that points to the EQ occurrence. The red band around the best fit is the 95% confidence interval, while the pink band is the 95% prediction band. (For interpretation of the references to colour in this figure legend, the reader is referred to the web version of this article.)

CRediT authorship contribution statement

A. De Santis: Funding acquisition, Conceptualization, Supervision, Methodology, Writing – original draft, Writing – review & editing. **L. Perrone:** Funding acquisition, Methodology, Writing – review & editing. **M. Calcara:** Investigation, Writing – review & editing. **S.A. Campuzano:** Methodology, Software, Validation, Writing – review & editing. **G. Cianchini:** Methodology, Software, Validation, Writing – review & editing. **S. D'Arcangelo:** Visualization, Investigation, Writing – review & editing. **D. Di Mauro:** Investigation, Writing – review & editing. **D. Marchetti:** Software, Validation, Visualization, Writing – review & editing. **A. Nardi:** Investigation, Writing – review & editing. **M. Orlando:** Software, Validation, Visualization, Writing – review & editing. **A. Piscini:** Software, Validation, Visualization, Writing – review & editing. **D. Sabbagh:** Software, Validation, Visualization, Writing – review & editing. **M. Soldani:** Software, Validation, Visualization, Writing – review & editing.

Declaration of Competing Interest

We, authors of the present paper, declare that there is no conflict of interest.

Data availability

data are available at weblink given in the manuscript

Acknowledgements

This work was undertaken in the framework of Limadou-Science+ funded by ASI (Italian Space Agency). Part of the funds were also given by Working Earth (Pianeta Dinamico) Project. We thank GeoNet (NZ) for providing TEC data (we also thank Claudio Cesaroni and Luca Spogli for giving suggestions on TEC data analyses) and the Kyoto World Data Center for Geomagnetism (http://wdc.kugi.kyoto-u.ac.jp/) for providing geomagnetic data indices. ESA is thanked for providing the Swarm satellite data and the CNSA (Chinese National Space

Administration) for providing CSES-01 satellite data.

Appendix A. Supplementary data

Supplementary data to this article can be found online at https://doi.org/10.1016/j.rse.2022.113325.

References

Akhoondzadeh, M., De Santis, A., Marchetti, D., Piscini, A., Cianchini, G., 2018. Multi precursors analysis associated with the powerful Ecuador (MW = 7.8) earthquake of 16 april 2016 using swarm satellites data in conjunction with other multi-platform satellite and ground data. Adv. Space Res. 61, 1, 248–263. https://doi.org/10.1016/j.asr.2017.07.014.

Akhoondzadeh, M., De Santis, A., Marchetti, D., Piscini, A., Jin, S., 2019. Anomalous seismo-LAI variations potentially associated with the 2017 Mw=7.3 Sarpol-e Zahab (Iran) earthquake from Swarm satellites, GPS-TEC and climatological data. Adv. Space Res. 64, 1, 143–158. https://doi.org/10.1016/j.asr.2019.03.020.

Benioff, H., 1949. Seismic evidence for the fault origin of oceanic deeps. GSA Bull. 60 (12), 1837–1856. https://doi.org/10.1130/0016-7606(1949)60[1837:SEFTFO]2.0.CO;2.

Bertello, I., Piersanti, M., Candidi, M., Diego, P., Ubertini, P., 2018. Electromagnetic field observations by the DEMETER satellite in connection with the 2009 L'Aquila earthquake. Ann. Geophys. 36, 1483–1493. https://doi.org/10.5194/angeo-36-1483-2018.

Bondur, V.G., Gokhberg, M.B., Garagash, I.A., Alekseev, D.A., 2020. Revealing short-term precursors of the strong M > 7 earthquakes in Southern California from the simulated stress-strain state patterns exploiting geomechanical model and seismic catalog data. Front. Earth Sci. 8, 571700 https://doi.org/10.3389/feart.2020.571700.

Bowman, D.D., Ouillon, G., Sammis, C.G., Sornette, A., Sornette, D., 1998. An observational test of the critical earthquake concept. J. Geophys. Res. 103 (B10), 24. https://doi.org/10.1029/98JB00792.

Bufe, C.G., Varnes, D.J., 1993. Predictive modelling of the seismic cycle of the greater San Francisco Bay region. J. Geophys. Res. 98, 9871–9883.

Carbone, V., Piersanti, M., Materassi, M., Battiston, R., Lepreti, F., Ubertini, P., 2021. A mathematical model of lithosphere-atmosphere coupling for seismic events. Sci. Rep. 11, 8682. https://doi.org/10.1038/s41598-021-88125-7.

Cesaroni, C., Spogli, L., Alfonsi, L., De Franceschi, G., Ciraolo, L., Monico, J.F.G., Scotto, C., Romano, V., Aquino, M., Bougard, B., 2015. L-band scintillations and calibrated total electron content gradients over Brazil during the last solar maximum. J. Space Weather Space Clim. 5, A36. https://doi.org/10.1051/swsc/2015038.

Chiodini, G., Cardellini, C., Amato, A., Boschi, E., Caliro, S., Frondini, F., Ventura, G., 2004. Carbon dioxide earth degassing and seismogenesis in central and southern Italy. Geophys. Res. Lett. 31 (L07615), 1–4. https://doi.org/10.1029/2004GL019480.

Chiodini, G., Cardellini, C., Di Luccio, F., Selva, J., Frondini, F., Caliro, S., Rosiello, A., Beddini, G., Ventura, G., 2020. Correlation between tectonic CO2 earth degassing and seismicity is revealed by a 10-year record in the apennines, Italy. Sci. Adv. 6 (35), eabc2938. https://doi.org/10.1126/sciadv.abc2938.

Cianchini, G., De Santis, A., Di Giovambattista, R., et al., 2020. Revised accelerated moment release under test: fourteen worldwide real case studies in 2014–2018 and simulations. Pure Appl. Geophys. 177, 4057–4087. https://doi.org/10.1007/s00024-020-02461-9.

Ciraolo, L., Azpilicueta, F., Brunini, C., Meza, A., Radicella, S.M., 2007. Calibration errors on experimental slant total electron content (TEC) determined with GPS. J. Geod. 81 (2), 111–120.

Cussac, T., Clair, M.-A., Ultré-Guerard, P., Buisson, F., Lassalle-Balier, G., Ledu, M., Elisabelar, C., Passot, X., Rey, N., 2006. The Demeter microsatellite and ground segment, planetary and space science 413–427 (5), 0032–0633. https://doi.org/10.1016/j.pss.2005.10.013.

D'Arcangelo, S., Bonforte, A., De Santis, A., Maugeri, S.R., Perrone, L., Soldani, M., Arena, G., Brogi, F., Calcara, M., Campuzano, S.A., Cianchini, G., Del Corpo, A., Di Mauro, D., Fidani, C., Ippolito, A., Lepidi, S., Marchetti, D., Nardi, A., Orlando, M., Piscini, A., Regi, M., Sabbagh, D., Zhima, Z., Yan, R., 2022. A Multi-Parametric and Multi-Layer Study to Investigate the Largest 2022 Hunga Tonga–Hunga Ha'apai Eruptions. Remote Sensing. 14 (15), 3649. https://doi.org/10.3390/rs14153649.

Dascher-Cousineau, K., Lay, T., Brodsky, E.E., 2020. Two foreshock sequences post gulia and wiemer (2019). Seismol. Res. Lett. 91, 2843–2850.

De Santis, A., Cianchini, G., Di Giovambattista, R., 2015. Accelerating moment release revisited: examples of application to italian seismic sequences. Tectonophysics 639, 82–98. https://doi.org/10.1016/j.tecto.2014.11.015.

De Santis, A., Balasis, G., Pavón-Carrasco, F.J., Cianchini, G., Mandea, M., 2017. Potential earthquake precursory pattern from space: the 2015 Nepal event as seen by magnetic swarm satellites. Earth Planet. Sci. Lett. 461, 119–126.

De Santis, A., Marchetti, D., Spogli, L., Cianchini, G., Pavón-Carrasco, F.J., De Franceschi, G., Di Giovambattista, R., Perrone, L., Qamili, E., Cesaroni, C., et al., 2019a. Magnetic field and electron density data analysis from swarm satellites searching for ionospheric effects by great earthquakes: 12 case studies from 2014 to 2016. Atmosphere 10, 371. https://doi.org/10.3390/atmos10070371.

De Santis, A., Cianchini, G., Qamili, E., Frepoli, A., 2010. The 2009 L'Aquila (Central Italy) seismic sequence as a chaotic process. Tectonophysics 496 (1–4), 44–52. https://doi.org/10.1016/j.tecto.2010.10.005.

De Santis, A., Marchetti, D., Pavón-Carrasco, F.J., Cianchini, G., Perrone, L., Abbattista, C., Alfonsi, L., Amoruso, L., Campuzano, S.A., Carbone, M., Cesaroni, C., De Franceschi, G., De Santis, A., Di Giovambattista, R., Ippolito, A., Piscini, A., Sabbagh, D., Soldani, M., Santoro, F., Spogli, L., Haagmans, R., 2019b. Precursory worldwide signatures of earthquake occurrences on swarm satellite data. Sci. Rep. 9, 20287. https://doi.org/10.1038/s41598-019-56599-1.

De Santis, A., Abbattista, C., Alfonsi, L., Amoruso, L., Campuzano, S.A., Carbone, M., Cesaroni, C., Cianchini, G., De Franceschi, G., De Santis, A., Di Giovambattista, R., Marchetti, D., Martino, L., Perrone, L., Piscini, A., Rainone, M.L., Soldani, M., Spogli, L., Santoro, F., 2019c. Geosystemics view of earthquakes. Entropy 21 (4), 412. https://doi.org/10.3390/e21040412.

De Santis, A., Cianchini, G., Marchetti, D., Piscini, A., Sabbagh, D., Perrone, L., Campuzano, S.A., Inan, S., 2020. A multiparametric approach to study the preparation phase of the 2019 M7.1 Ridgecrest (California, USA) Earthquake. Front. Earth Sci. 8, 478. https://doi.org/10.3389/feart.2020.540398.

De Santis, A., Marchetti, D., Perrone, L., Campuzano, S.A., Cianchini, G., Cesaroni, C., Di Mauro, D., Orlando, M., Piscini, A., Sabbagh, D., Soldani, M., Spogli, L., Zhima, Z., Shen, X., 2021. Statistical correlation analysis of strong earthquakes and ionospheric electron density anomalies as observed by CSES-01. Nuovo Cimento C 2021, 4–5. https://doi.org/10.1393/ncc/i2021-21119-1.

Dobrovolsky, I.P., Zubkov, S.I., Miachkin, V.I., 1979. Estimation of the size of earthquake preparation zones. PAGeoph. 117, 1025. https://doi.org/10.1007/BF00876083.

Felzer, K.R., Abercrombie, R.E., Ekström, G., 2004. A common origin for aftershocks, foreshocks, and multiplets. Bull. Seismol. Soc. Am. 94 (1), 88–98.

Finlay, C.C., Kloss, C., Olsen, N., et al., 2020. The CHAOS-7 geomagnetic field model and observed changes in the South Atlantic anomaly. Earth Planets Space 72, 156. https://doi.org/10.1186/s40623-020-01252-9.

Freund, F., 2011. Pre-earthquake signals: underlying physical processes. J. Asian Earth Sci. 383–400.

Gelaro, R., McCarty, W., Suárez, M.J., Todling, R., Molod, A., Takacs, L., Randles, C.A., Darmenov, A., Bosilovich, M.G., Reichle, R., Wargan, K., Coy, L., Cullather, R., Draper, C., Akella, S., Buchard, V., Conaty, A., da Silva, A.M., Gu, W., Kim, G.-K., Koster, R., Lucchesi, R., Merkova, D., Nielsen, J.E., Partyka, G., Pawson, S., Putman, W., Rienecker, M., Schubert, S.D.C., Sienkiewicz, M., Zhao, B., 2017. The Modern-Era Retrospective Analysis for Research and Applications, Version 2 (MERRA-2). Journal of Climate 30 (14), 5419–5454. https://doi.org/10.1175/JCLI-D-16-0758.1.

Gulia, L., Wiemer, S., 2019. Real-time discrimination of earthquake foreshocks and aftershocks. Nature 574, 193–199. https://doi.org/10.1038/s41586-019-1606-4.

Hayakawa, M., Molchanov, O.A., 2002. Seismo Electromagnetics Lithosphere-Atmosphere-Ionosphere Coupling (ed. TERRAPUB) 477 pages, Tokyo.

Herrmann, M., Piegari, E., Marzocchi, W., 2022. Revealing the spatiotemporal complexity of the magnitude distribution and b-value during an earthquake sequence. Nat. Commun. 13, 5087. https://doi.org/10.1038/s41467-022-32755-6.

Liperovsky, V.A., Meister, C.-V., Liperovskaya, E.V., Davidov, V.F., Bogdanov, V.V., 2005. On the possible influence of radon and aerosol injection on the atmosphere and ionosphere before earthquakes. Natural Hazards and Earth System Sciences 5 (6), 783–789. https://doi.org/10.5194/nhess-5-783-2005.

Liu, Q., De Santis, A., Piscini, A., Cianchini, G., Ventura, G., Shen, X., 2020a. Multi-parametric climatological analysis reveals the involvement of fluids in the preparation phase of the 2008 ms 8.0 wenchuan and 2013 ms 7.0 lushan earthquakes. Remote Sens. 12, 1663. https://doi.org/10.3390/rs12101663.

Liu, Q., Shen, X., Zhang, J., Cui, J., Tan, Q., Zhao, S., Li, M., 2020b. Aerosol anomalies associated with occurrence of recent strong earthquakes (> M 8.0). Terr. Atmos. Ocean. Sci. 31, 677–689. https://doi.org/10.3319/TAO.2020.05.22.01.

Marchetti, D., De Santis, A., Shen, X., Campuzano, S.A., Perrone, L., Piscini, A., Di Giovambattista, R., Jin, S., Ippolito, A., Cianchini, G., Cesaroni, C., Sabbagh, D., Spogli, L., Zhima, Z., Huang, J., 2019. Possible lithosphere-atmosphere-ionosphere coupling effects prior to the 2018 Mw=7.5 Indonesia earthquake from seismic, atmospheric and ionospheric data. J. Asian Earth Sci. https://doi.org/10.1016/j.jseaes.2019.104097.

Marchetti, D., De Santis, A., Campuzano, S.A., Soldani, M., Piscini, A., Sabbagh, D., Cianchini, G., Perrone, L., Orlando, M., 2020. Swarm Satellite Magnetic Field Data Analysis Prior to 2019 Mw = 7.1 Ridgecrest (California, USA) Earthquake 12, 502. https://doi.org/10.3390/geosciences10120502.

McGuire, J.J., Boettcher, M.S., Jordan, T.H., 2005. Foreshock sequences and short-term earthquake predictability on East Pacific rise transform faults. Nature 434, 457–461. https://doi.org/10.1038/nature03377.

Mignan, A., 2011. Retrospective on the Accelerating Seismic Release (ASR) hypothesis: Controversy and new horizons. Tectonophysics 505 (1–4), 1–16. https://doi.org/10.1016/j.tecto.2011.03.010.

Mogi, K., 1963. Some discussions on aftershocks, foreshocks and earthquake swarms – the fracture of a semi-infinite body caused by inner stress origin and its relation to the earthquake phenomena (3). Bull. Earthquake Res. Inst. Univ. Tokyo 41, 615–658.

Mueller, S.C., 2019. Earthquake Catalogs for the USGS National Seismic Hazard Maps. Seismological Research Letters 90 (1), 251–261. https://doi.org/10.1785/0220170108.

Nanjo, K.Z., Yoshida, A., 2021. Changes in the b value in and around the focal areas of the M6.9 and M6.8 earthquakes off the coast of Miyagi prefecture, Japan, in 2021. Earth Planets Space 73, 176. https://doi.org/10.1186/s40623-021-01511-3.

Okal, E.A., 2019. Energy and magnitude: a historical perspective. Pure Appl. Geophys. 176, 3815–3849. https://doi.org/10.1007/s00024-018-1994-7.

Parrot, M., 2002. The micro-satellite DEMETER. J. Geodynam. 33 (4–5), 535–541. https://doi.org/10.1016/S0264-3707(02)00014-5.

Parrot, M., 2012. Statistical analysis of automatically detected ion density variations recorded by DEMETER and their relation to seismic activity. Ann. Geophys. 55 (1). https://www.annalsofgeophysics.eu/index.php/annals/article/view/5270.

Picozza, P., Conti, L., Sotgiu, A., 2021. Looking for earthquake precursors from space: a critical review. Front. Earth Sci. 14 https://doi.org/10.3389/feart.2021.676775.

Piersanti, M., Materassi, M., Battiston, R., Carbone, V., Cicone, A., D'Angelo, G., Diego, P., Ubertini, P., 2020. Magnetospheric–Ionospheric–Lithospheric coupling model. 1: observations during the 5 august 2018 bayan earthquake. Magnetospheric-ionospheric-lithospheric coupling model 1. Remote Sens. 12 (20), 3299. https://doi.org/10.3390/rs12203299.

Pinheiro, K.J., Jackson, A., Finlay, C.C., 2011. Measurements and uncertainties of the occurrence time of the 1969, 1978, 1991, and 1999 geomagnetic jerks. Geochem. Geophys. Geosyst. 12, Q10015.

Piscini, A., De Santis, A., Marchetti, D., Cianchini, G., 2017. A multi-parametric climatological approach to study the 2016 amatrice-norcia (Central Italy) earthquake preparatory phase. Pure Appl. Geophys. 174 (10), 3673–3688.

Piscini, A., Marchetti, D., De Santis, A., 2019. Multi-parametric climatological analysis associated with global significant volcanic eruptions during 2002–2017. Pure and Appl. Geoph. 176 (8), 3629–3647. (https://link.springer.com/article/10.1007%2Fs00024-019-02147-x).

Pulinets, S., Ouzounov, D., 2011. Lithosphere–atmosphere–ionosphere coupling (LAIC) model-an unified concept for earthquake precursors validation. J. Asian Earth Sci. 41 (4–5), 371–382. https://doi.org/10.1016/j.jseaes.2010.03.005.

Pulinets, S., Tsidilina, M., Ouzounov, D., Davidenko, D., 2021. From Hector mine M7.1 to ridgecrest M7.1 earthquake. A look from a 20-year perspective. Atmosphere 12, 262. https://doi.org/10.3390/atmos12020262.

Qin, K., Wu, L.X., De Santis, A., Meng, J., Ma, W.Y., Cianchini, G., 2012. Quasi-synchronous multi-parameter anomalies associated with the 2010–2011 New Zealand earthquake sequence. Nat. Hazards Earth Syst. Sci. 12, 1059–1072. https://doi.org/10.5194/nhess-12-1059-2012.

Scholz, C.H., 2015. On the stress dependence of the earthquake b value. Geophys. Res. Lett. 42 (5), 1399–1402. https://doi.org/10.1002/2014GL062863.

Shannon, C.E., 1948. A mathematical theory of communication. Bell Syst. Tech. J. 27, 379–423.

Shen, X., Zhang, X., Yuan, S., et al., 2018. The state-of-the-art of the China seismo-electromagnetic satellite mission. Sci. China Technol. Sci. 61, 634–642. https://doi.org/10.1007/s11431-018-9242-0.

Smith, E.M.I., Price, R.C., 2006. The Tonga-kermadec arc and Havre-lau back-arc system: their role in the development of tectonic and magmatic models for the western Pacific, J. Volcanol. Geothermal Res. 156. 3–4, 315–331. https://doi.org/10.1016/j.jvolgeores.2006.03.006.

Sorokin, V.M., Yashchenko, A.K., Surkov, V.V., 2019. Generation of geomagnetic disturbances in the ionosphere by a tsunami wave. Geomagn. Aeron. 59, 221–233. https://doi.org/10.1134/S0016793219020130.

Tributsch, H., 1978. Do aerosol anomalies precede earthquakes? Nature 276, 606–608. https://doi.org/10.1038/276606a0.

Wang, Q., Huang, J.P., Zhang, X.M., Shen, X.H., Yuan, S.G., Zeng, L., Cao, J.B., 2018. China seismo-electromagnetic satellite search coil magnetometer data and initial results. Earth and Planetary Physics 2 (6), 462–468. https://doi.org/10.26464/epp2018044.

Wiemer, S., 2000. Minimum magnitude of completeness in earthquake catalogs: examples from Alaska, the Western United States, and Japan. Bull. Seismol. Soc. Am. 90 (4), 859–869. https://doi.org/10.1785/0119990114.

Zhima, Z., Huang, J., Shen, X., Chen, L., Piersanti, M., Yang, Y., Wang, Q., Zeng, L., Lei, J., Chu, W., Zhao, S., Hu, Y., Guo, F., 2020. Simultaneous observations of ELF/VLF rising-tone quasiperiodic waves and energetic electron precipitations in the high-latitude upper ionosphere. J. Geophys. Res. Space. Physics Volume 125, Issue 5. https://doi.org/10.1029/2019JA027574.

Zhu, F., Jiang, Y., 2020. Investigation of GIM-TEC disturbances before M $\geq$ 6.0 inland earthquakes during 2003–2017. Sci. Rep. 10, 18038. https://doi.org/10.1038/s41598-020-74995-w.